

# **Nanostructured Materials Supported Oxygen Reduction Catalysts in Polymer Electrolyte Membrane Fuel Cells**

by

Ja-Yeon Choi

A thesis

presented to the University of Waterloo

in fulfillment of the

thesis requirement for the degree of

Master of Applied Science

in

Chemical Engineering

Waterloo, Ontario, Canada, 2013

© Ja-Yeon Choi 2013

## **Author's Declaration**

I hereby declare that I am the sole author of this thesis. This is a true copy of the thesis, including any required final revisions, as accepted by my examiners.

I understand that my thesis may be made electronically available to the public.

## **Abstract**

Polymer electrolyte membrane (PEM) fuel cells have been viewed as promising power source candidates for transport, stationary, and portable applications due to their high efficiency and low emissions. The platinum is the most commonly used catalyst material for the oxygen reduction reaction (ORR) at the cathode of PEM fuel cells; however, the limited abundance and high cost of platinum hinder the large-scale commercialization of fuel cells. To overcome this limitation, it is necessary to enhance the catalyst utilization in order to improve the catalytic activity while decreasing or eliminating the use of platinum.

The material on which the catalyst is supported is important for the high dispersion and narrow distribution of Pt nanoparticles as well as other non-precious metal active sites, and these characteristics are closely related to electrocatalytic activity of the catalysts. The support materials can influence the catalytic activity by interplaying with catalytic metals, and the durability of the catalyst is also greatly dependent on its support. A variety of support materials like carbons, oxides, carbides, and nitrides have been employed as supports materials for fuel cell catalysts, and much effort has been devoted to the synthesis of the novel carbon supports with large surface area and/or pore volume, including nanostructured carbons such as carbon nanotubes (CNTs), carbon nanofibers, and mesoporous carbon. For example, carbon nanotube supported Pt catalysts have shown improved catalytic activity and durability compared to the commercial catalyst supported on Vulcan XC-72 carbon black, due to the structural and electrical properties of CNTs. Mesoporous carbon supported Pt catalysts also have shown excellent performance in PEM

fuel cell electrode reactions, attributed to the high uniform dispersion of catalytic metals, the high electrical conductivity, and the enhanced mass transfer due to the pore structure of the materials. The carbon support can also be doped by other atoms or compounds in order to obtain both improved catalytic activity and enhanced durability for ORR. These novel nanostructured carbon materials have achieved promising performance in terms of catalytic activity and durability. However, there is still enormous demand and potential for the catalysts to improve.

In the first study, non-precious metal catalysts (NPMC) for the oxygen reduction reaction were synthesized by deposition of Fe/Co-N<sub>x</sub> composite onto nanoporous carbon black with ethylenediamine (EDA) as nitrogen precursor. Two different nanoporous carbon supports, Ketjen Black EC300J (KJ300) and EC600JD (KJ600), were used as catalyst support for the non-precious catalysts. The results obtained from the optimized FeCo/EDA-carbon catalyst, using KJ600 as the support, showed improved onset, half-wave potentials and superior selectivity than that of the KJ300. Similarly, the catalyst showed good performance in the hydrogen-oxygen PEM fuel cell. At a cell voltage of 0.6 V the fuel cell managed to produce 0.37 A/cm<sup>2</sup> with a maximum power density of 0.44 W/cm<sup>2</sup>. Fuel cell life test at a constant voltage of 0.40 V demonstrated promising stability up to 100 h. The X-ray photoelectron spectroscopy study indicated that pyridinic type nitrogen of the non-precious metal catalysts is critical for ORR catalytic activity and selectivity. These results suggest higher pore volume and surface area of carbon support could lead to higher nitrogen content providing more active sites for ORR and this type of catalyst has great potential used as a non-precious PEM fuel cell catalyst

In the second study, we report the development of a novel NPMC in acid electrolyte using pyrimidine-2,4,5,6-tetramine sulfuric acid hydrate (PTAm) as a nitrogen precursor and graphene nanosheets as catalyst supports. Graphene, consisting of a two-dimensional (2D) monolayer of graphitic carbon atoms, has been viewed as a promising candidate for the fuel cell catalyst support, due to its many intriguing properties such as high aspect ratios, large surface areas, rich electronic states, good electron transport, thermal/chemical stability and good mechanical properties. We investigate the effect of different pyrolysis temperatures on the catalysts' ORR activity along with detailed surface analysis to provide insight regarding the nature of the ORR active surface moieties. This novel NPMC demonstrates promising electrocatalyst activity and durability superior to that of commercial catalyst for the ORR, rendering graphene nanosheets as a suitable replacement to traditional nanostructured carbon support materials.

In the final study, we have developed Pt catalyst by combining the precious metal with nitrogen-doped activated graphene (N-AG) as the support. A transmission electron microscopy (TEM) image of the catalyst shows uniform size and distribution of platinum nanoparticles on a graphene layer. This novel catalyst demonstrates superior electrocatalyst activity and durability over Pt/XC72 catalyst for ORR under the studied conditions, rendering graphene as an ideal replacement to traditional nanostructured carbon support materials.

In summary, several catalyst samples were made using novel nanostructured support materials to improve the ORR performance. Several recommendations for future work were suggested in the last section of this work to further apply the knowledge and understanding

of nanostructured support materials to design a highly active, durable, and low-cost NPMCs and platinum catalysts.

## **Acknowledgements**

This work reported herein was financially supported by the Natural Sciences and Engineering Research Council of Canada (NSERC), and University of Waterloo.

I would like to acknowledge the support from Dr. Zhongwei Chen and my colleagues, Ryan Hsu, Clark Chen, Drew Higgins, and Jason Wu in producing this work.

# Table of Contents

List of Figures .....	xi
List of Tables.....	xiv
List of Acronyms.....	xv
Section 1: Introduction.....	1
1.1 Problem Statement.....	1
1.2 Operation Principle.....	2
1.3 Technical Challenges.....	4
1.4 Nanostructured Support Materials.....	6
1.4.1 Non-Precious Metal Catalysts.....	6
1.4.2 Platinum Based Catalysts.....	8
1.5 Organization of Thesis .....	9
Section 2: Characterization Techniques.....	10
2.1 Physical Characterization Techniques.....	10
2.1.1 Scanning Electron Microscopy/Energy Dispersive X-Ray.....	10
2.1.2 Transmission Electron Microscopy .....	13
2.1.3 X-Ray Diffraction .....	15
2.1.4 X-Ray Photoelectron Spectroscopy .....	16
2.1.5 Brunauer-Emmett-Teller Analysis .....	17
2.2 Electrochemical Characterization Techniques .....	18
2.2.1 Rotating Disc and Ring Disc Electrode .....	18
2.2.2 Membrane Electrode Assembly Testing .....	24
Section 3: Mesoporous Carbon Supported Non-Precious Catalyst.....	28
3.1 Introduction and Motivation.....	28

3.2	Experimental.....	30
3.2.1	Catalyst Synthesis .....	31
3.2.2	Characterization .....	32
3.2.3	Electrocatalytic Activity Evaluation .....	33
3.2.4	MEA Preparation .....	33
3.2.5	Fuel Cell Measurements.....	34
3.3	Results and Discussion .....	35
3.4	Conclusions .....	49
Section 4: Graphene Nanosheets Supported Non-precious Catalyst .....		51
4.1	Introduction and Motivation.....	51
4.2	Experimental.....	54
4.2.1	Synthesis of Fe-PTAm/G .....	54
4.2.2	Physical Characterization.....	54
4.2.3	Rotating Ring Disc Electrode Experiments .....	55
4.3	Results and Discussion .....	56
4.4	Conclusions .....	66
Section 5: Nitrogen-doped Activated Graphene Supported Platinum Electrocatalyst.....		68
5.1	Introduction and Motivation.....	68
5.2	Experimental.....	69
5.2.1	Activated Graphene Synthesis .....	69
5.2.2	Catalyst Preparation .....	71
5.2.3	Electrocatalytic Activity Evaluation .....	72
5.3	Results and Discussion .....	72
5.4	Conclusions .....	82
Section 6: Summary and Future Work.....		83

References ..... 86  
Appendix ..... 95

## List of Figures

Figure 1: A diagram illustrating the operation principles of aPEM fuel cell device. ....	2
Figure 2: Schematic of a typical scanning electron microscope and imaging process. ....	11
Figure 3: Schematic representation of a column in a transmission electron microscope. ....	14
Figure 4: An illustration of an electrochemical half-cell RDE setup. ....	19
Figure 5: Schematic representation of a RRDE head from a top view .....	20
Figure 6: A set of ORR curves with different rotation speeds .....	22
Figure 7: Typical MEA polarization curve with a power density versus current density plot .....	25
Figure 8: Sample polarization curve with various polarization losses in a fuel cell.....	26
Figure 9: Schematic representation for preparation of the FeCo-EDA-C catalyst. ....	30
Figure 10: XRD patterns for functionalized KJ300, KJ600, FeCo-EDA-KJ300R and FeCo- EDA-KJ600R. ....	36
Figure 11: ORR curves of a) FeCo-EDA-300R and b) FeCo-EDA-600R at various rotation speed in 0.5M H <sub>2</sub> SO <sub>4</sub> electrolyte. ....	39
Figure 12: ORR curves of various catalysts; FeCo-EDA-KJ300, FeCo-EDA-KJ600, FeCo- EDA-KJ300R and FeCo-EDA-KJ600R, obtained at 900 rpm in 0.5M H <sub>2</sub> SO <sub>4</sub> . ....	40
Figure 13: Hydrogen peroxide yield for various catalysts obtained at 900rpm in 0.5M H <sub>2</sub> SO <sub>4</sub> ; FeCo-EDA-300, FeCo-EDA-600, FeCo-EDA-300R and FeCo-EDA-600R.....	42
Figure 14: The fractional yield of hydrogen peroxide for four samples; FeCo-EDA-KJ300, FeCo-EDA-KJ600, FeCo-EDA-KJ300R and FeCo-EDA-KJ600R.....	43
Figure 15: XPS spectrum of FeCo-EDA-KJ300R and FeCo-EDA-KJ600R showing all the elements in the samples.....	45

Figure 16: XPS spectrum showing the presence of different types of nitrogen groups from the N 1s signal.....	46
Figure 17: Polarization curve and corresponding power densities of MEAs fabricated with FeCo-EDA-KJ600R cathode catalyst and commercially available catalyzed GDE anode. Cell temperature: 80°C; Catalyst loading: 4 mg/cm <sup>2</sup> ; H <sub>2</sub> /O <sub>2</sub> back pressures: 30 psi/30 psi. ....	48
Figure 18: Durability test of the H <sub>2</sub> /O <sub>2</sub> PEM fuel cell at 0.4V for 100 hours. MEA was fabricated with FeCo-EDA-KJ600R catalyst and commercially available catalyzed GDE as the cathode and anode respectively. Cathode catalyst loading: 4 mg/cm <sup>2</sup> ; Cell temperature: 80°C; No back pressure. ....	49
Figure 19: (a) Proposed schematic representation of the coupling reaction of pyrimidine-2,4,5,6-tetramine sulfuric acid hydrate to graphene nanosheets. (b) Two TEM images of Fe-PTAm/Graphene pyrolyzed at 800°C, obtained at different magnifications. ....	53
Figure 20: (a) ORR curves of Fe-PTAm/Graphene catalysts heat-treated in N <sub>2</sub> using different pyrolysis temperatures, obtained at 900 rpm. (b) ORR curves of FPG800 at various rotation speeds. ....	57
Figure 21: H <sub>2</sub> O selectivity for the Fe-PTAm/Graphene catalysts, obtained at 900 rpm.....	59
Figure 22: ORR curves of FPG800 before and after running 1000 CV cycles in nitrogen saturated electrolyte. ....	61
Figure 23: XPS summary of surface atomic composition of Fe-PTAm/Graphene catalysts.	62
Figure 24: N 1s narrow scan spectra of the various FPG samples.....	65
Figure 25: Nitrogen content of the various FPG samples.....	66

Figure 26: Schematic representation of activated nitrogen-doped graphene support synthesis .....	71
Figure 27: XRD patterns of Pt/XC72 and Pt/N-AG.....	73
Figure 28: High resolution TEM images of (a) Pt/AG and (b) Pt/N-AG catalysts illustrating Pt nanoparticles and their distribution on the graphene supports. ....	75
Figure 29: ORR curves of Pt catalysts supported on N-AG, AG and XC72 obtained at 900 rpm in oxygen saturated 0.1 M HClO <sub>4</sub> electrolyte with a potential scan rate of 10 mV/s. ....	77
Figure 30: a) The ORR performance of Pt/N-AG catalyst in various rotating speed and b) the Koutecky-Levich plot obtained in oxygen saturated 0.1 M HClO <sub>4</sub> electrolyte with a potential scan rate of 10 mV/s.....	78
Figure 31: High resolution TEM images of (a) Pt/N-AG and (b) Pt/XC72 catalysts after accelerated durability test.....	80
Figure 32: ORR curves of Pt/N-AG and Pt/XC72 before and after accelerated durability test obtained at 900 rpm in oxygen saturated 0.1 M HClO <sub>4</sub> electrolyte with a potential scan rate of 10 mV/s.....	81

## List of Tables

Table 1: Summary of physical properties of Ketjen Black EC300J and EC600JD .....	31
Table 2: EDX elemental analysis of FeCo-EDA-300R and FeCo-EDA-600R samples.. .....	37
Table 3: Half-wave and onset potential vs. RHE of FeCo-EDA-300, FeCo-EDA-600, FeCo-EDA-300R and FeCo-EDA-600R.....	41
Table 4: XPS analysis of the elemental composition of FeCo-EDA-300R and FeCo-EDA-600R .....	46
Table 5: Summary of RRDE experiments for synthesized catalyst samples. ....	60
Table 6: The mean platinum particle size of Pt/XC72 and Pt/N-AG.....	74

## List of Acronyms

BET	Brunauer Emmett and Teller
DOE	U.S. Department of Energy
EDA	Ethylenediamine
EDX	Energy Dispersive X-Ray
GDE	Gas Diffusion Electrode
KJ300	Ketjenblack EC-300J
KJ600	Ketjenblack EC-600JD
MEA	Membrane Electrode Assembly
NPMC	Non-Precious Metal Catalyst
OCV	Open Circuit Voltage
ORR	Oxygen Reduction Reaction
PEM	Polymer Electrolyte Membrane
PTAm	Pyrimidine-2,4,5,6-tetramine sulfuric acid hydrate
RDE	Rotating Disc Electrode
RHE	Reversible Hydrogen Electrode
RRDE	Rotating Ring Disc Electrode
SEM	Scanning Electron Microscopy
TEM	Transmission Electron Microscopy
XPS	X-Ray Photoelectron Spectroscopy
XRD	X-Ray Diffraction

## **Section 1: Introduction**

### **1.1 Problem Statement**

With world's rapid increasing demand for energy and rising awareness for environmental issues, the need for sustainable and environmentally benign energy technology is getting urgent on a global level. The world primary energy consumption is expected to grow by more than 30% from 2013 to 2030, and several studies have indicated that the reserve for the crude oil and gas, the main fossil fuel resources for world energy supply, will near an end within the next 50 years[1, 2]. As one of the most promising renewable energy technologies to replace the fossil fuels and resolve the rising demand issues, fuel cells, particularly proton exchange membrane (PEM) fuel cells are becoming increasingly popular due to its high energy conversion efficiency, high power density, and environmental benignity. PEM fuel cells are regarded as a very important technology possessing a great potential for various applications including transportation power, micropower, stationary power and other generation applications[3]. However, despite the advantages and focus on the technology, system cost of existing PEM fuel cells are still very high; the majority of the cost comes from the use of platinum in the electrodes, especially for the oxygen reduction reaction (ORR) at the cathode of PEM fuel cells, hindering the large-scale commercialization of fuel cells[4]. To overcome this limitation, low cost catalysts with higher activity and durability for ORR must be developed.

## 1.2 Operation Principle

Fuel cells refer to devices that convert chemical energy in fuels into electrical energy. There are many types of fuel cells that use a wide variety of fuels and oxidants, but the most common type and of most interest are the fuel cells that use hydrogen and oxygen as the reductant and the oxidant, respectively. In a typical hydrogen/oxygen fuel cell including PEM fuel cell, two gases are supplied into the fuel cell's electrodes, where on anode side the hydrogen is catalyzed generating protons and electrons and on the cathode side protons are combined with oxygen to form water, as illustrated in Figure 1.

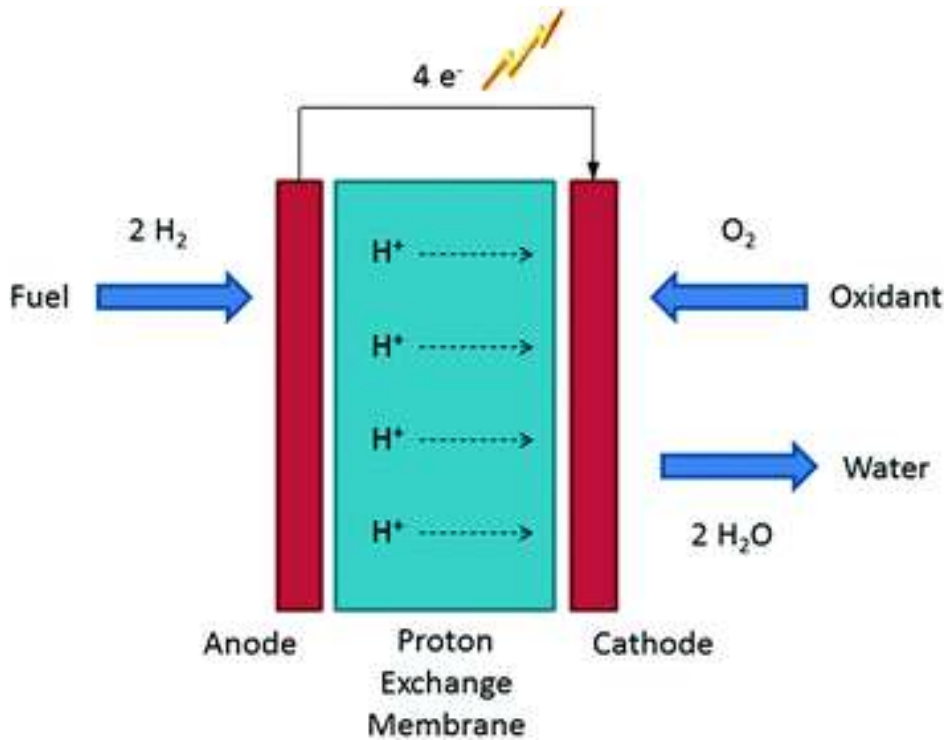


**Figure 1: A diagram illustrating the operation principles of a PEM fuel cell device. Reproduced with permissions from [5]. Copyright © 2010 Springer**

The hydrogen gas purged at the anode side undergoes the half-cell reaction described in Equation 1.



Where  $E^0$  is the standard half-cell potential based on a reversible hydrogen electrode (RHE). By dissociating a hydrogen gas molecule, two protons and two electrons are generated from this reaction. The electrons travel through the external circuit whereas the protons migrate through the polymer electrolyte membrane inside the cell. Both electrons and protons reach the cathode where they react to combine with the supplied oxygen fuel and form water, following another half-cell reaction as shown in Equation 2 [6].



By combining the above two equations together, it gives the overall reaction described in Equation 3:



In principle, the only products from this overall fuel cell reaction are water and heat, which makes the fuel cell considered as zero-emission, thus environmentally friendly energy device[6]. The Equation 3 can be balanced to show a reaction involving a single oxygen molecule with four protons and four electrons combine to form two water molecules, which is normally referred as 4-electron pathway as described in Equation 4.



Ideally, fuel cells can generate power as long as there is continuous supply of each fuel assuming no other side reactions and no catalysts or other components degradation. However, besides the most common and most preferred 4-electron pathway reaction, another reaction that generates electrons is usually observed simultaneously as shown in Equation 5. This reaction is referred as 2-electron pathway where an oxygen molecule with two protons and two electrons combine to form a hydrogen peroxide.



The generation of hydrogen peroxide by the 2-electron pathway not only lowers the energy conversion efficiency but also can damage the internal components of the fuel cell by forming harmful radical species[6]. Thus, the degree of the two different pathway reactions should be investigated while evaluating new catalysts and the development of the catalysts should be targeted so that it favors the 4-electron pathway.

### **1.3 Technical Challenges**

As described in the operation principle, two half-reactions occur in the process of generating energy in the fuel cell, and it is known that the reaction happening at the cathode side is prone to high overpotential and slow reaction kinetics compared to the other at the anode, thus becoming the rate limiting reaction [7-9]. This leads to the higher amount of platinum required for the cathode than the anode side, and research efforts have been focusing on

reducing or eliminating the platinum loading on the cathode catalysts. Two main ideas proposed to solve this issue are: 1) decreasing the platinum loading on catalysts, and 2) developing non-precious metal catalysts (NPMC) that are active for ORR [9].

There are several different techniques that are employed or have been proposed to reduce the platinum loading. The main principle applied is to enhance the platinum utilization by increasing the electrochemically active surface area of the platinum per mass base. One popular method on which ample amount of research is being done recently is alloying platinum with different metals to increase the exposed Pt surface area and/or bringing out positive synergetic effects such as enhanced stability and ORR activity [10-15]. Another method is use carbon support in various forms to disperse platinum nanoparticles uniformly on the surface while preventing dissolution or aggregation of the particles [16-18].

While decreasing the platinum loading on catalysts would likely bring the desired performance and reduced cost in short amount of time, utilizing platinum will eventually bring up the system cost again and make the device less sustainable due to the rising price of platinum. Instead, although their performances are still not par as that of platinum catalysts, eliminating the use of platinum and developing NPMCs by using other transition metal to form active sites have been considered as long term solution [6, 19].

In this thesis, both NPMCs and platinum based catalysts have been developed and investigated by using different nanostructured support materials.

## **1.4 Nanostructured Support Materials**

### **1.4.1 Non-Precious Metal Catalysts**

It was seemed among the scientists that only precious metal catalysts were active for ORR until the early work in 1964 by Jasinski who first discovered that cobalt phthalocyanine was able to reduce oxygen in alkaline media [20, 21]. In 1989, Yeager applied a heat treatment in the presence of nitrogen and transition-metal precursors to achieve a reasonable performance at lower material cost [21]. Since then, the idea of using non-precious metal in the ORR catalyst have drawn a lot of attention in the field of fuel cell catalysts and there has been a significant progress in the performance improvement and understanding of the ORR mechanism on NPMCs.

Despite the ample amount of research being done in the field of NPMCs, it is still unclear as to what kind of active sites exist and of which type is most active. Along with the high temperature heat treatment, it has generally been accepted that a metal precursor is necessary to achieve a reasonable ORR activity. Metal free catalysts for PEM fuel cell application also have been developed in the past, however, the performance achieved is far lower than the ones with metal precursor involved during the synthesis. Some researchers support the idea that the active site exist in the form of Fe-N<sub>x</sub> complex, while others claim that the metal precursors only assist in forming the active site but not participate directly in the ORR reaction [22]. Several different types of metals have been studied to work in creating the ORR active catalysts, including Fe [23-30], Co [26-29, 31-35], Ni [27, 31, 34, 36, 37] and

Cu [27, 31, 34, 36, 38]. From these findings, the general trend is that Fe tends to show the highest activity among the other non-precious metal precursor. The Co precursor often results in achieving high activity but its durability is poor due to the dissolution in acid media. The optimal loading suggested of these metal precursors is usually very low, ranging from 0.2 to 2 wt.% for the best performance [9]. The metal precursor loading higher than 4 wt.% will most likely lead to forming agglomerates that cause negative outcome upon high-temperature heat treatment as well as can easily dissolve in an ink or electrolyte solution.

Not only the presence of metal precursors but it is also crucial to use nitrogen precursor in synthesizing NPMCs. Many different types of nitrogen precursors have been studied and have been utilized successfully in creating ORR active catalysts. It seems that the more nitrogen content the better the ORR performance it gets, although not many have achieved nitrogen loading over 4 wt.% after high temperature treatment over 700°C. Some of the popular nitrogen precursors include ethylenediamine [22, 39-43], polyaniline [26, 44, 45], polyacrylonitrile [27, 35, 46-48], acetonitrile [37, 46, 49], and ammonia [50-56].

The carbon support also serves as one of the key factors to influence the overall catalyst performance. Carbon black has been intensively used as a catalyst support due to its low cost, abundance, chemical property, easy-to handle, and electroconductivity [30]. However, with technology development in preparing many novel or low-cost nanostructured materials, many types of carbon supports have also been utilized as support material for the fuel cell catalysts including mesoporous carbons [50, 57-60], carbon nanotubes [61-66], and carbon nanofibres [25, 67-69]. These support materials benefit from having high specific area that are prospective regions for active sites formation and also having high electroconductivity.

In general, the key factors in achieving high ORR activity seem to be utilizing carbon supports with disordered contents and micropores, while having fairly low amount of Fe precursor and high nitrogen content after synthesis. More detailed information is provided regarding the carbon support materials, precursors and synthesis methods in the main sections.

#### **1.4.2 Platinum Based Catalysts**

The material on which the catalyst is supported is important for the high dispersion and narrow distribution of Pt nanoparticles, and these characteristics are closely related to electrocatalytic activity of the catalysts[64]. The support materials can influence the catalytic activity by interplaying with catalytic metals, and the durability of the catalyst is also greatly dependent on its support[70]. A variety of support materials like carbons, oxides, carbides, and nitrides have been employed as supports materials for Pt[71-76], and much effort has been devoted to the synthesis of the novel carbon supports with large surface area and pore volume, including nanostructured carbons such as carbon nanotubes (CNTs), carbon nanofibers, and mesoporous carbon[25, 39, 61, 65, 67, 77, 78]. For example, nanostructured carbon supported Pt catalysts have shown improved catalytic activity and durability compared to the commercial catalyst supported on Vulcan XC-72 carbon black, due to the structural and electrical properties of CNTs[66]. Mesoporous carbon supported Pt catalysts also have shown excellent performance in PEM fuel cell electrode reactions, attributed to the high uniform dispersion of catalytic metals, the high electrical conductivity, and the

enhanced mass transfer due to the pore structure of the materials[58, 60]. The carbon support can also be doped by other atoms or compounds in order to obtain both improved catalytic activity and enhanced durability for ORR[62, 79, 80]. These novel nanostructured carbon materials have achieved promising performance in terms of catalytic activity and durability. However, there is still enormous demand and potential for the catalysts to improve.

## **1.5 Organization of Thesis**

This thesis explores a several novel approaches utilized for the design and synthesis of fuel cell catalysts with nanostructured supports for the oxygen reduction reaction (ORR) that are critical for the functionality of a PEM fuel cell. The thesis is divided into six sections. The first section introduced the reader to the scope and objectives of the work as well as background information in fuel cell catalysis. Section 1 contains a literature review on past work done in the field of catalysts for fuel cells. Section 2 discusses most of the theory and analysis techniques that were utilized in the work done for this thesis. The three experiments utilizing mesoporous, graphene nanoplatelets, and graphene supports are described in Sections 3, 4 and 5 respectively. These sections describe the motivation for the work, the experimental procedure, the discussion of the results and the conclusions arrived at. The work described in sections 3 and 4 have been published previously as well as most part of the work 5. Section 6 summarizes the important results and some discussion on the future direction that the work may take.

## **Section 2: Characterization Techniques**

To verify the functionality and to investigate the performance of synthesized catalysts, electrochemical measurements are required. However, in order to fully understand the possible reasons for the outcome and to be able to further apply the discovered knowledge into future studies, various physical characterization techniques must be utilized. This section will illustrate the details regarding several physical and electrochemical characterization techniques that are applied in the research present in this thesis.

### **2.1 Physical Characterization Techniques**

The types of physical characterization techniques discussed in the following section are scanning electron microscopy (SEM), energy dispersive X-ray (EDX), transmission electron microscopy (TEM), X-ray diffraction (XRD), X-ray photoelectron spectroscopy (XPS), and Brunauer-Emmett-Teller (BET) analysis.

#### **2.1.1 Scanning Electron Microscopy/Energy Dispersive X-Ray**

Scanning Electron Microscopy (SEM) is one of the most reliable methods for analyzing solid materials [81]. It is a type of electron microscopy that captures images of the surface of sample by scanning it with high-energy beam of electrons. Since the emitted electrons have smaller wavelength than photons, SEM can achieve higher magnification than optical microscopes and thus very sensitive. Due to this reason the operation requires the sample to

be placed under ultra-high vacuum. The emitted electrons hit the atoms of the sample and their bombardment and interactions with the sample will produce various types of signals, including secondary electrons, back scattered electrons, characteristic X-rays[82]. This happens due to the varying energy levels of the incident electrons. They all contain useful information about the sample's morphology, surface topography, compositions, crystallography and other important physical properties. The schematic representation of a typical SEM is illustrated in Figure 2.

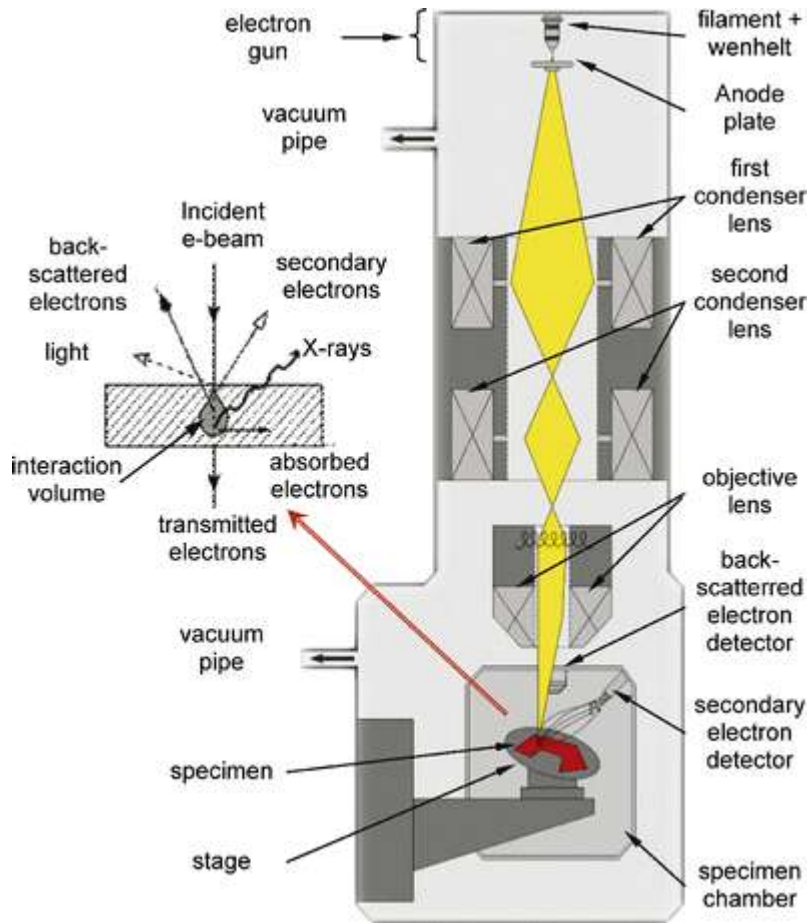


**Figure 2: Schematic of a typical scanning electron microscope and imaging process. Reproduced with permissions from [83]. Copyright © 2010 Springer**

Electron Gun: Main component of cathode, held at high positive potential, to knock off electrons

Anode: Held at high negative potential with respect to the cathode, which helps accelerating the electrons down the column.

Condenser Lens : The condenser lens is magnetic lens where it utilizes magnetic field to refocus the electrons. Both 1<sup>st</sup> and 2nd set of condenser lens remove the high angle electrons and reform the electrons into a more coherent beam.

Object Lens: The magnetic lens refocuses the beam, and the objective aperture filters out high angle electrons in order to control the final spot size of the electron beam on the sample.

Specimen Chamber: Where the electron beam and the sample interaction takes place.

Stage: To move sample in and out, rotate in plane, and allow user to switch from one sample to the other.

Backscattering Electron Detector: Placed directly above the sample and collects the backscattered electrons.

Secondary Electron Detector: Usually a detector mounted to the side of the sample stage, positively biased to detect secondary electrons emitted from the surface.

SEM can be coupled with energy dispersive X-ray (EDX) analysis to determine elemental composition as well as other properties such as electroconductivity of a sample. EDX is based on the characteristic X-rays emitted by scattering of incident electrons with the sample. Since EDX collects the characteristic X-rays, it provides compositional information of the sample. For a typical EDX spectrum, it plots the X-ray emission lines of element on the x-axis and the percent composition of those lines on the y-axis.

### **2.1.2 Transmission Electron Microscopy**

Transmission electron microscopy (TEM) is a technique where a beam of electrons is transmitted through and interacts with an ultra-thin specimen [84]. The schematic showing the inner structure of a conventional TEM is shown in Figure 3. The electrons are generated by a process called thermionic emission from a tungsten filament and are aligned and accelerated as they pass through numerous intermediate and projector lenses [85]. An image will be formed from the electrons transmitted through the specimen and it will be magnified and focused by an objective lens. The image produced is the result of beam electrons that are scattered by the specimen versus those that are not.

The main difference between SEM and TEM is the structural information about the sample material they deliver. While SEM is mainly used to visualize the surface topography and morphology of the material sample, TEM is widely used to study the underlying inner structures of the sample material.

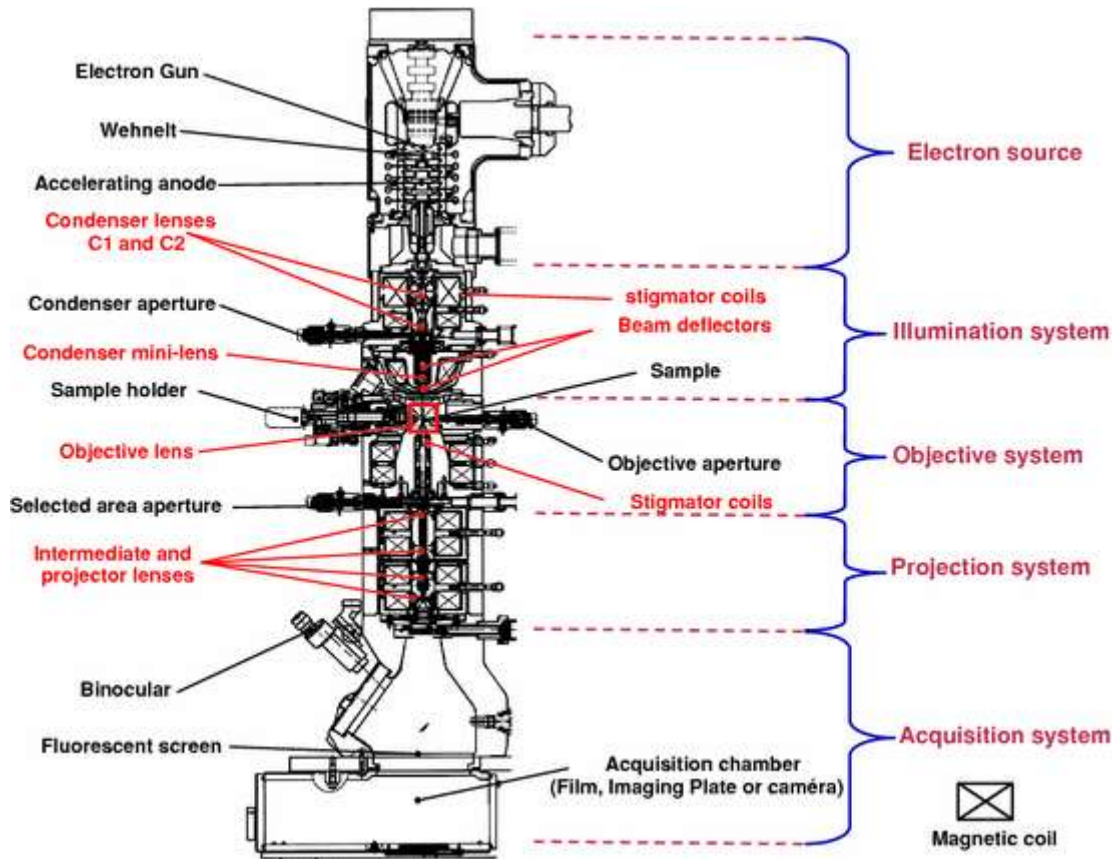


**Figure 3: Schematic representation of a column in a transmission electron microscope. Reproduced with permissions from [86]. Copyright © 2010 Springer**

TEM is also capable of getting much higher resolution than optical microscopes or SEM due to the small de Broglie wavelength of electrons. The Equation 6 gives the maximum resolution achieved by an optical microscope given the wavelength of a photon.

$$d = \frac{\lambda}{2n \sin \alpha} \quad (6)$$

Where  $\lambda$  is the wavelength of photon,  $n$  is a positive integer, and  $d$  is the theoretical maximum resolution. If we apply the de Broglie wavelength of electrons, this maximum resolution will increase to a degree that the instrument can distinguish objects in a few nanometer range.

In this study, TEM was utilized to view the surface morphology of the catalyst support materials, to verify the presence of metal particles, and to observe the size of the platinum particles deposited onto the carbon support.

### **2.1.3 X-Ray Diffraction**

X-ray Diffraction (XRD) is a non-destructive characterization technique that identifies the crystalline phases in materials and measures the structural properties such as chemical composition, grain size, and etc [87]. It also determines the thickness of thin films and atomic arrangements in amorphous materials. There are several types of X-ray diffraction such as single crystal X-ray diffraction, powder diffraction, thin-film diffraction, and high-resolution XRD.

A beam of monochromatic X-rays of known wavelength will be generated by the filament X-ray tubes, by striking an anode (Cu in this case) of a particular metal with high-energy electrons. The incident X-Rays will pass through divergence limiting slit, bombard the sample at a certain angle and reach the detector through a receiving slit. Interaction of X-rays with sample creates secondary diffracted beams of X-rays that are related to interplanar spacings in the powder, according to Bragg's Law (Equation 7):

$$n \lambda = 2d \sin \theta \quad (7)$$

Where  $n$  is an integer,  $\lambda$  is wavelength of X-rays,  $d$  is the interplanar spacing, and  $\theta$  is the diffraction angle. The information given by the reflected X-rays is based on the atomic structure of the sample materials which is caused by the elastic scattering of X-rays from the electron clouds of the species within the sample [88].

From XRD spectra, the mean platinum particle size can be easily estimated from Scherrer's equation (Equation 8)

$$d = K\lambda / (B \cos\theta) \quad (8)$$

Where  $d$  is the particle diameter (nm),  $K$  is the shape factor,  $\lambda$  is the wavelength of the x-rays (0.154 nm for Cu-K $\alpha$ ),  $B$  is the full width at half-maximum (FWHM) of the peak of the interest in radian and  $\theta$  is the Bragg angle of the peak in degrees.

In this study, XRD was applied to obtain the morphology and crystallinity of the carbon materials, to identify the presence and state of metal as well as to analyze the mean size of the platinum particles along with the results obtained from TEM images.

#### **2.1.4 X-Ray Photoelectron Spectroscopy**

X-ray photoelectron spectroscopy (XPS) is a quantitative technique that measures elemental composition, chemical states, and electronic states existing in the sample material. The XPS spectra are obtained by irradiating the sample with a beam of X-rays while measuring the number of electrons and the kinetic energy from the material [89].

Conventional XPS instruments utilize a highly focused 20 to 200  $\mu\text{m}$  beams of monochromatic aluminum K-alpha X-rays. Due to the sensitivity of the instrument and to accurately detect the number of electrons, the device must be operated in an ultra-high vacuum to minimize any source of error. XPS can only analyze materials with their atomic numbers equal to or greater than 3 since the orbitals in hydrogen or helium are too small. This spectroscopy technique is commonly used for materials such as inorganic compounds, metal alloys, semiconductors, polymers, ceramics, catalysts, and etc [90, 91].

In this work, XPS was utilized to analyze the surface concentrations of various elements including iron, nitrogen and carbon on the catalysts. It was also used to quantify the different types of nitrogen-carbon bonds existing on the catalysts to see which structure is mostly related to the electrocatalytic active sites.

### **2.1.5 Brunauer-Emmett-Teller Analysis**

Brunauer-Emmett-Teller (BET) analysis utilizes the physical adsorption of gases onto solid materials to measure the specific surface area of the solid. The theory works based on a number of assumptions; adsorption occurs only on well-defined sites of the sample, there is no interaction between the adsorption layers, and the layer number tend to go infinity at the saturation pressure [92].

BET analysis is very useful for obtaining structural information on the catalyst and its support, especially when the material is porous. The principle of nanotechnology is to increase the reaction sites by increasing the area to volume ratio to achieve superior

performance or functionality, thus the specific surface area measured by BET analysis can possibly become a significant source of evidence. In this work, BET analysis was utilized to measure the specific surface areas and pore distributions in the raw carbon black support materials and the catalysts synthesized in this study.

## **2.2 Electrochemical Characterization Techniques**

To verify the functionality and to investigate the performance of synthesized catalysts, electrochemical measurements are required. The following two sections explain about half-cell measurement of the catalyst and complete fuel cell test.

### **2.2.1 Rotating Disc and Ring Disc Electrode**

Both the rotating disc electrode (RDE) experiment and rotating ring disc electrode (RRDE) experiment are one of the most widely used electrochemical characterization technique to test activity of catalysts in the field of fuel cell and air-battery. The main difference between the two is that the RRDE has an ability to test hydrogen peroxide generation during the test. The system simulates one of the two electrodes of the fuel cell depending on the supplied gas, but since the cathode catalyst is of the most interest, mainly the cathodic reaction occurs at the tip of the RDE with the supply of oxygen as the fuel. Two other connections, counter electrode and reference electrode are necessary to complete the circuit with the tip of the RDE as the working electrode. All three electrodes are in contact with the electrolyte and a continuous flow of oxygen in the system keeps the electrolyte saturated. The main

advantage of using this method over the complete fuel cell test is that it can save cost and time taking to assemble a full cell to test the performance of a newly synthesized catalyst, by evaluating in a simple and easy-to-handle setup. The schematic illustration for the complete RDE/RRDE system is shown in Figure 4.

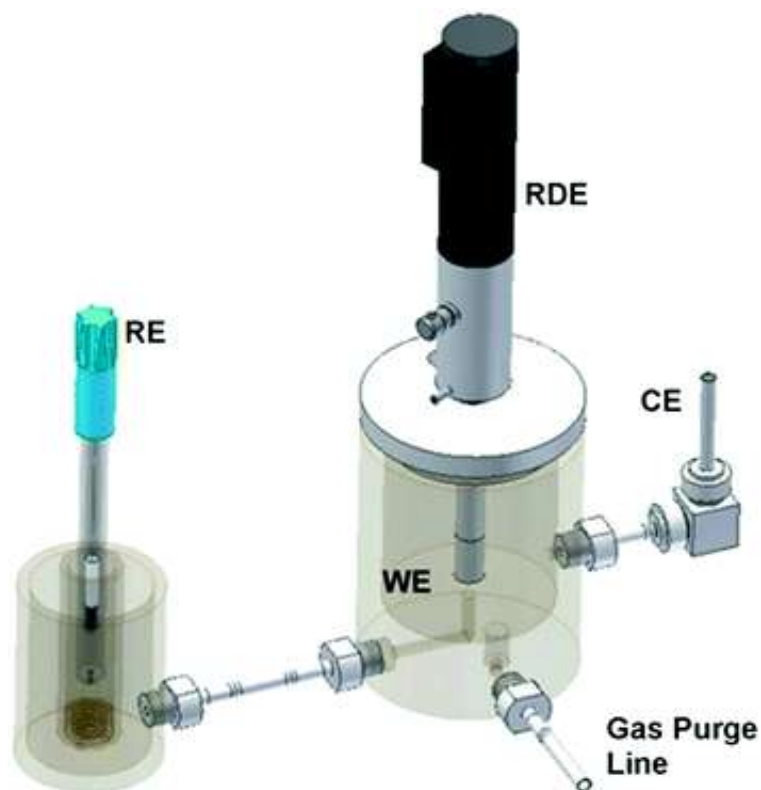


**Figure 4: An illustration of an electrochemical half-cell RDE setup. Reproduced with permissions from [5]. Copyright © 2010 Springer**

The common type of RDE used in fuel cell catalyst test has a round disc made of glassy carbon, where the sample catalyst ink will be deposited and form a catalyst layer once dried. The rotation feature of this electrode is important since it helps the mass transfer of the oxygen to the electrode surface by creating a laminar flow in the cell. While RDE can carry

out most electrochemical measurement on the fuel cell catalyst that are currently being practiced, RRDE adds another ring-type working electrode made of platinum, surrounding the glassy carbon disc. This enables the system to capture a portion of the hydrogen peroxide being generated and give information on the selectivity of the catalyst. The surface schematic of the RRDE is shown in Figure 5.

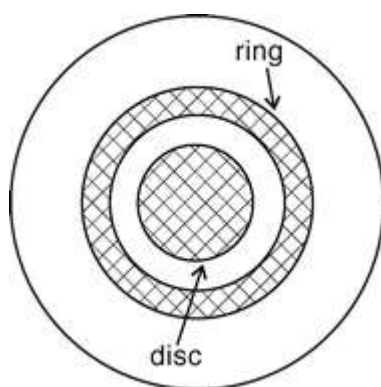


**Figure 5: Schematic representation of a RRDE head from a top view. Reproduced with permissions from [93]. Copyright © 2010 Springer**

Reduction of oxygen by two different pathways generates  $\text{H}_2\text{O}$  and  $\text{H}_2\text{O}_2$  simultaneously at the working electrode, and due to the laminar flow all the products are pushed away from the glassy carbon towards the ring. When the ring electrode is held at a certain voltage, it can reduce the  $\text{H}_2\text{O}_2$  to  $\text{H}_2\text{O}$  and the current change is monitored at the second working electrode. With this information it is possible to analyze the number of electrons transferred during ORR and the percentage of 2-electron pathway reaction over the 4-electron pathway

reaction based on the current density difference. This selectivity can be calculated by the following equations [6]:

$$n = 4|I_D| / (|I_D| + (|I_R|/N)) \quad (9)$$

$$\%H_2O_2 = 100(4 - n)/2 \quad (10)$$

$$\%H_2O = 100 - \%H_2O_2 \quad (11)$$

Where  $n$  is the number of electrons transferred,  $I_D$  is the current from the disc electrode,  $I_R$  is the current from the ring electrode,  $N$  is the collection efficiency which is usually indicated by the manufacturer of the instrument,  $\%H_2O_2$  is the selectivity of  $H_2O_2$  and  $\%H_2O$  is the selectivity of  $H_2O$ .

The rate of rotation changes the current of the laminar flow which is correlated to the amount of saturated solution to reach the catalyst surface in a given time. Increase in the rotation speed means higher rate of fuel being supplied at the reaction site. A typical RDE test is done by scanning the potential of the working electrode in a selected range while monitoring the current behavior as plotted in Figure 6. A plot of current density versus potential for a certain range is called ORR curve, and these curves are usually obtained at a set of rotation speeds of 100, 400, 900, 1600 rpm or higher in  $O_2$  saturated acid electrolyte.

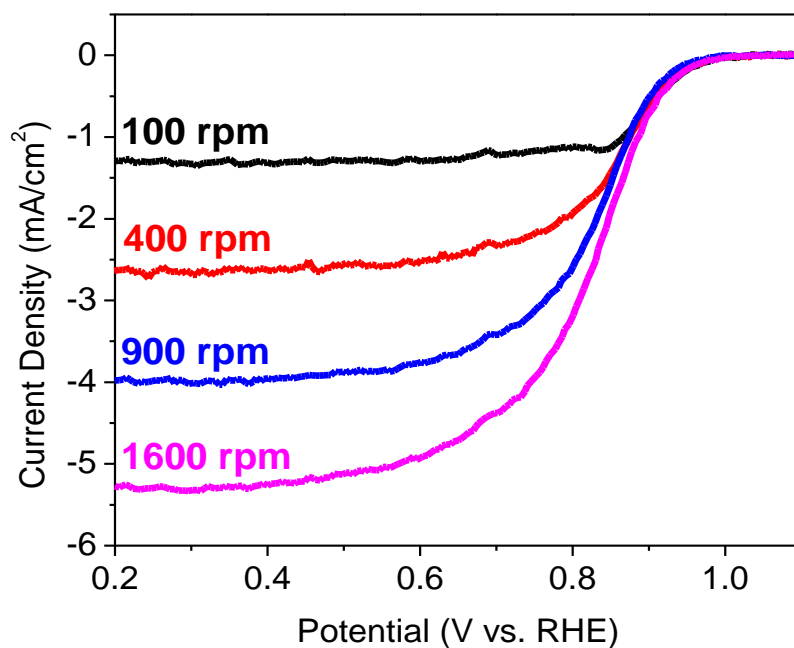


**Figure 6: A set of ORR curves with different rotation speeds. Reproduced with permissions from [94]. Copyright © 2012 ECS – The Electrochemical Society**

At a point where the oxygen reduction reaction initiates, this potential is called onset potential. From this potential to the point where the overpotential of the reaction does not increase the current density, the reaction is governed by its kinetics [6]. The current density in this kinetic limited region is modeled by Equation 12:

$$|i_k| = nFAk_f C \quad (12)$$

Where  $i_k$  is the reaction kinetics controlled current density,  $n$  is the number of electrons transferred,  $F$  is the Faraday constant,  $A$  is the area of the electrode,  $k_f$  is a rate constant as a function of the overpotential, and  $C$  is the reactant concentration in the bulk solution.

The current obtained at the region in which the current density does not increase upon changing potential is called the limiting current, where the mass transfer is the limiting factor. The model that describes this steady-state diffusion-controlled system is called the Levich equation and is shown in Equation 13.

$$|i_d| = 0.620nFAD^{2/3}\omega^{1/2}\nu^{-1/6}C \quad (13)$$

Where  $i_d$  is the diffusion controlled current density,  $n$  is the number of electrons transferred,  $F$  is the Faraday constant,  $A$  is the area of the electrode,  $D$  is the diffusion coefficient of reactant in the bulk solution,  $\omega$  is the angular rate of rotation,  $\nu$  is the kinematic viscosity, and  $C$  is the reactant concentration.

When the catalyst is deposited on the glassy carbon electrode, the ink usually contains Nafion which forms a layer binding the catalyst. The model that describes the diffusion behavior of reactant through the Nafion binding film is shown in Equation 14:

$$|i_f| = nFAC_f D_f / \delta \quad (14)$$

Where  $i_f$  is the diffusion current density of the reactant through the Nafion,  $n$  is the number of electrons,  $F$  is the Faraday's constant,  $A$  is the area of the electrode,  $C_f$  is the

concentration of reactant in the Nafion film,  $D_f$  is the diffusion coefficient of the reactant through the film, and  $\delta$  is the thickness of the Nafion layer.

The above three equations can be combined to model the overall current density at a specific potential in the diffusion layer near the surface of the electrode. This overall expression for current density is called the Koutecky-Levich equation and is described in Equation 15:

$$\frac{1}{|i|} = \frac{1}{|i_d|} + \frac{1}{|i_k|} + \frac{1}{|i_f|} \quad (15)$$

Where  $i$  is the overall or total current density,  $i_d$  is the diffusion controlled current density,  $i_k$  is the reaction kinetics controlled current density, and  $i_f$  is the diffusion current density of the reactant through the Nafion.

In this work, RRDE was utilized to characterize the onset potential, half-way potential, limiting current density, and/or  $H_2O/H_2O_2$  selectivity of the synthesized catalysts. RRDE was also used to investigate the durability of catalysts by repeated cyclic tests.

### 2.2.2 Membrane Electrode Assembly Testing

Although the half-cell measurement using the RRDE system is cost and time effective way to test the electrocatalytic activity of catalysts, the information given by the half-cell is limited. The actual fuel cell performance using the catalyst can be quite different than the half-cell test due to many other factors. To verify and see the actual fuel cell performance of the catalyst, membrane electrode assemblies (MEA) can be fabricated and tested in single

cell. After assembling the MEA stack, a polarization curve can be obtained by potential sweep as similar to that of the half-cell test. Many operating parameters can be adjusted including the flow rate for the hydrogen and oxygen, cell temperature, anode temperature, cathode temperature, relative humidity and etc. A typical polarization curve along the power density versus current density plot is shown in Figure 7, using platinum supported on carbon catalyst for both electrodes.

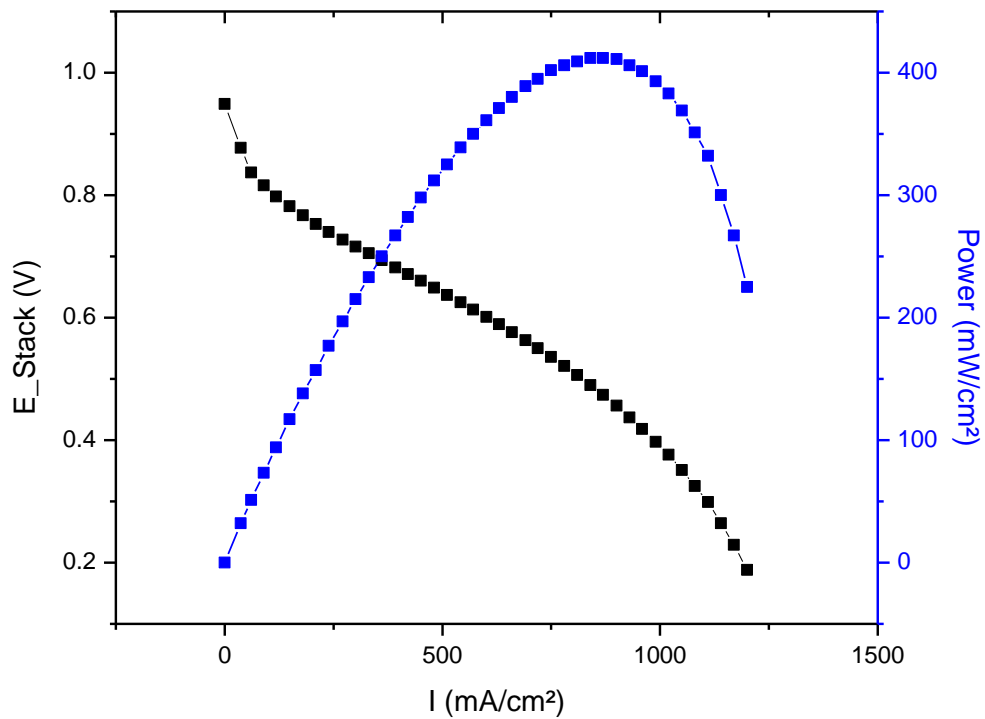


**Figure 7: Typical MEA polarization curve with a power density versus current density plot**

It is known that the theoretical maximum potential of one stack is 1.23V from the Equation 3. However, the measured potential at different current densities nor the open circuit voltage (OCV) do not reach the maximum value. These cell voltage loss has been studied and been categorized into three types of losses; activation (reaction rate) loss, ohmic (resistance) loss and concentration (gas transport) loss, as illustrated in Figure 8. The activation loss is mainly due to the sluggish kinetics of ORR on the cathode side in the low current density region. The ohmic loss takes effect throughout the whole current density range due to the resistance of electrons circulating through the system. Then in the high current density region, the mass transport becomes the limiting factor, causing the concentration loss.

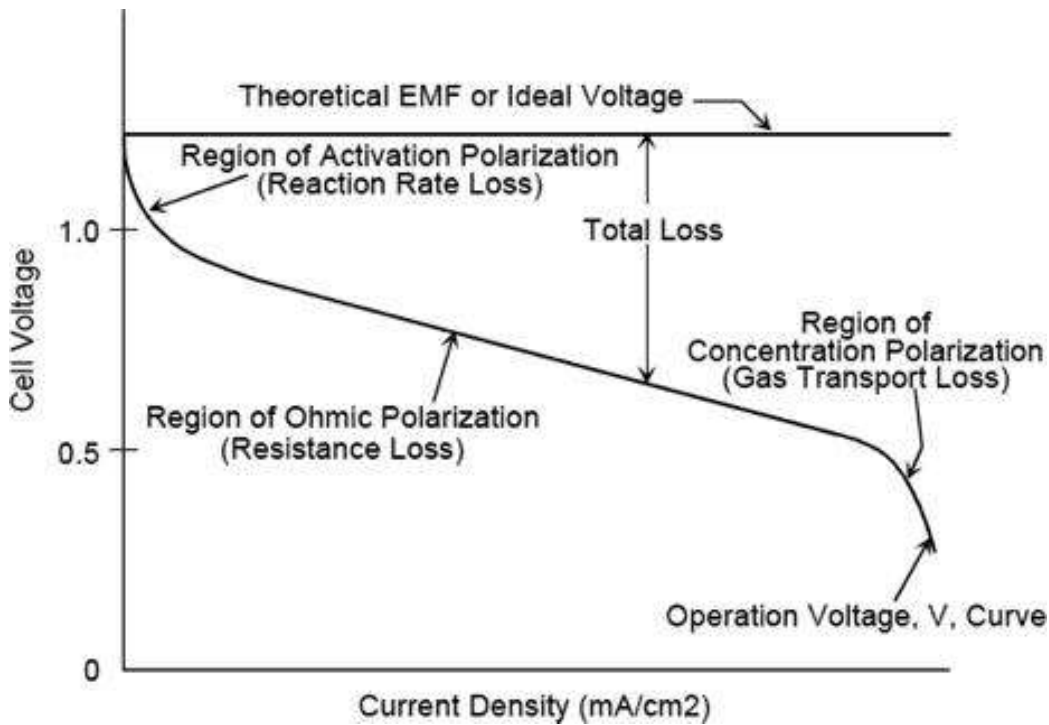


**Figure 8: Sample polarization curve with various polarization losses in a fuel cell**

By combining these three types of losses with the OCV, the total output voltage can be simulated as shown in the Equation 16.

$$E_{cell} = E_{OCV} - \Delta E_{act} - \Delta E_{ohmic} - \Delta E_{con} \quad (16)$$

Where  $E_{cell}$  is the output voltage of the cell,  $E_{OCV}$  is the open circuit voltage,  $\Delta E_{act}$  is the activation loss,  $\Delta E_{ohm}$  is the resistance loss, and  $\Delta E_{con}$  is the mass transfer loss.

MEA test was carried out in the first study in section 3 of this work, where the polarization curve was obtained for a NPMC synthesized with porous carbon support. Durability analysis utilizing MEA was also investigated. Specific parameters will be discussed in the experimental section in the following work.

## **Section 3: Mesoporous Carbon Supported Non-Precious Catalyst**

### **3.1 Introduction and Motivation**

The major limitation to hindering the activity of NPMCs is its low catalytic active site density[95]. Two major approaches have been proposed to overcome the limitation: 1) synthesize self-supported catalysts with high surface area, and 2) develop high surface area carbon supports with adequate pore sizes [96]. Many research papers discuss the performance of ORR catalysis by transition metal compounds which are formed in micropore structure, including the analysis of Fe-based catalysts by Dodelet and co-workers [95]. Dodelet et al. stated that two different catalytic sites, Me-N<sub>4</sub>-C (pyrrolic type) and Me-N<sub>2</sub>-C (pyridinic type) coexist in the catalysts, and these metal and nitrogen complexes bound to the carbon support is known to be catalytically active where the metal ion in the center of the macrosites plays a crucial role in ORR[97-106]. Recent papers published by Dodelet's group on the iron-based catalyst reported that the use of microporous carbon, Black Pearls 2000, has greatly increased the site density leading to an increase in the catalytic activity for ORR [107]. It has been proposed that the Me-N-C catalytic sites consist of a metal cation coordinated by either two or four nitrogen functionalities and are located at the edges of the opposite walls of the carbon micropores [108, 109]. Although there is controversy in literature regarding the active site and mechanism to ORR catalysis for these NPMCs, it is commonly accepted that the key to achieving higher activity is to increase the metal-nitrogen complexes by increasing the surface concentration of nitrogen groups on the

catalyst support. Based on these ideas, it can be concluded that there is a great potential to improve catalytic activity if the surface to volume ratio of micropores on the carbon support can be increased.

In this study, high performance NPMCs have been synthesized using Ketjen Black EC600JD (KJ600) as the carbon support, which possesses much higher pore volume and BET surface area than that of the commonly used Ketjen Black EC300J (KJ300) support (Table 1). On both KJ300 and KJ600 supports, metal/nitrogen complexes are deposited using EDA, followed by a high-temperature pyrolysis step, and chemical post-treatment. For metal additives, iron and cobalt are used as an agent to facilitate and stabilize the incorporation of nitrogen within the carbon matrix [110]. The schematic representation of the catalytic site formation in the pores of the carbon support is illustrated in Figure 9. The difference in ORR activity of the two catalysts will be discussed, and the relationship between the contents of different nitrogen groups present in the catalysts and the performance will be investigated.

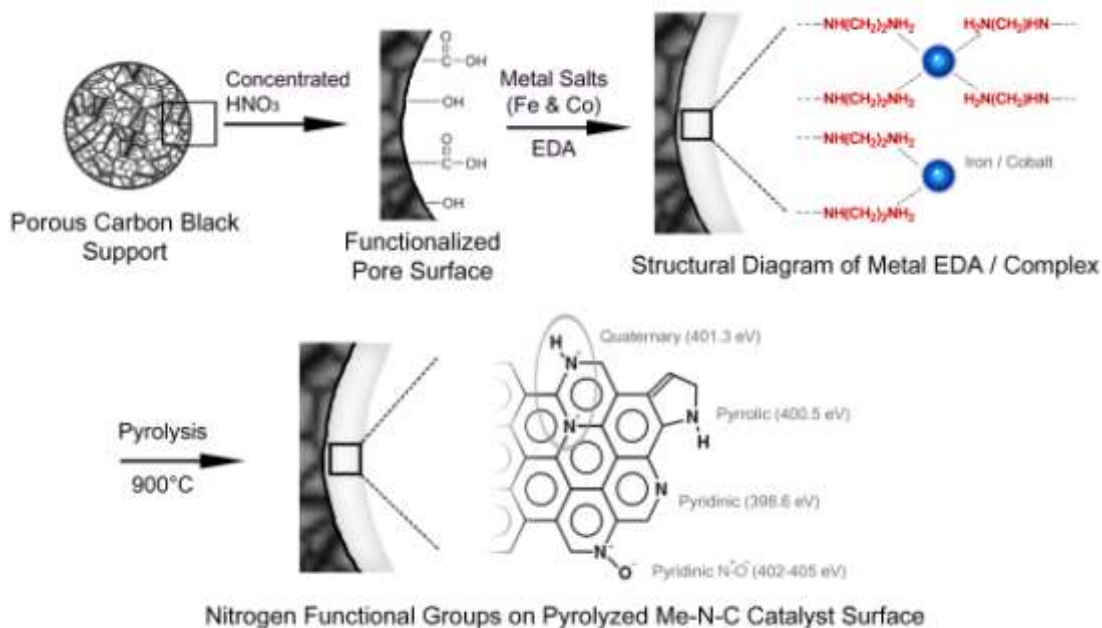


**Figure 9: Schematic representation for preparation of the FeCo-EDA-C catalyst. Reproduced with permissions from [39]. Copyright © 2010 American Chemistry Society**

### 3.2 Experimental

Two different catalysts have been synthesized using KJ300 and KJ600 supports. Physical and electrochemical characterization has been carried out on the sample catalyst products: FeCo-EDA-KJ300 and FeCo-EDA-KJ600. Two sets of samples were synthesized almost identically, the first set which did not undergo a reflux process (FeCo-EDA-300 and FeCo-EDA-600), and the second set which added a reflux during evaporation of ethanol (FeCo-EDA-300R and FeCo-EDA-600R), which show improved ORR activity over the samples synthesized without reflux.

Both Ketjen Black EC300J and EC600JD are porous carbon blacks suitable for electroconductive applications. Although KJ300 is known to have very high BET specific surface area (800 m<sup>2</sup>/g) compared to the conventional electroconductive blacks and is widely used as a fuel cell catalyst support, KJ600 has almost double the surface area of KJ300 (1400 m<sup>2</sup>/g), higher pore volume (480-510 mL/100 g) and also smaller particle size (34.0 nm), which can lead to significant increase in conductivity and performance of the resulting compound when combined with polymer complex. The physical properties of both carbon black supports are outlined in Table 1.

**Table 1: Summary of physical properties of Ketjen Black EC300J and EC600JD. Reproduced with permissions from [39]. Copyright © 2010 American Chemistry Society.**

	<b>KJ300</b>	<b>KJ600</b>	<b>FeCo-EDA-300R</b>	<b>FeCo-EDA-600R</b>
BET surface area (m <sup>2</sup> /g)	822.7	1416.2	312.1	483.7
Pore volume (cm <sup>3</sup> /g)	1.048	2.279	0.298	0.541
Average pore width (nm)	6.36	5.79	4.51	5.31

### 3.2.1 Catalyst Synthesis

Two types of carbon black graphite, KJ300 and KJ600, were treated in concentrated (6M) HCl solution to remove metal impurities present on the carbon. This was followed by thoroughly washing the carbon black with copious amounts of DE-IONIZED water before filtering and drying the carbon black overnight in an oven at 60°C. The remaining solid was subject to reflux in 70% HNO<sub>3</sub> solution at 80°C for 8 hours to introduce carboxyl groups

onto the carbon surface. The carbon black was then washed again with DE-IONIZED water, filtered and dried overnight in an oven at 60°C. 0.25 g of both  $\text{Co}(\text{NO}_3)_2 \cdot 6\text{H}_2\text{O}$  and  $\text{FeSO}_4 \cdot 7\text{H}_2\text{O}$  were fully dissolved in 125 mL of ethanol before adding 2 mL of ethylenediamine. This solution was stirred for half an hour, thus creating the ethylenediamine polymer complex. 0.5 g of functionalized carbon black which was synthesized previously was then dispersed in 125 mL of ethanol and added with the metal and ethylenediamine polymer complex solution. The combined solution was then boiled for an hour under ambient pressure with and without reflux. This boiling procedure was done under air at approximately 80°C in order to drive the polymerization. If reflux was used, it was then removed after an hour to allow the ethanol to evaporate completely. The remaining dried precipitate was ground and pyrolyzed at 900 °C for an hour, raising the temperature at 20 °C/min while supplying a constant flow of inert nitrogen gas. The sample was then acid treated in 0.5M  $\text{H}_2\text{SO}_4$  for 8 hours before being filtered and washed with 1 L of DE-IONIZED water. The sample was oven dried overnight at 80°C before use.

### **3.2.2 Characterization**

X-ray diffraction (XRD) data was obtained by using Inel XRG 3000 with  $\text{CuK}\alpha$  radiation to determine elemental composition of the catalysts. Energy dispersive X-ray spectroscopy (EDX) data was obtained by using a LEO1530 FE-SEM, equipped with EDAX Pegasus 1200 integrated EDX/OIM. X-ray photoelectron spectroscopy (XPS) data was obtained using Thermal Scientific K-Alpha XPS spectrometer in order to investigate the relative content of different elements in the catalyst sample.

### **3.2.3 Electrocatalytic Activity Evaluation**

Electrocatalytic activity was evaluated in a three-electrode electrochemical cell using a Pine-Instrument's Bipotentiostat AFCBP1, equipped with a speed rotator. The electrode was equipped with a 0.19635 cm<sup>2</sup> glassy carbon surface and a 5.0 mm diameter Pt ring (collection efficiency of 26%). All RRDE measurements were performed in acidic electrolyte; 0.5M H<sub>2</sub>SO<sub>4</sub>, using a Ag/AgCl reference electrode at room temperature. To prepare the electrode, 4 mg of sample was dissolved ultrasonically into 2 mL of ethanol before 20 L of the ink and 10 L of 0.05% Nafion solution were applied to the glassy carbon disk. Thus, the catalyst loading on the glass carbon electrode was approximately 20.4 mg/cm<sup>2</sup>. ORR curves were recorded in the potential range at a scan rate of 10 mV/s with the electrolyte saturated with oxygen gas. ORR curves were corrected for the background by conducting the same sweep voltammetry in the absence of oxygen and subtracting the curve from the measured ORR curves. Nitrogen was used as the inert gas which was with saturated in the electrolyte. The measurements were repeated at various rotation speeds (100, 400, 900 and 1600 rpm). The ring potential was maintained at 1.2 V vs. RHE throughout the experiments in order to oxidize H<sub>2</sub>O<sub>2</sub> produced during oxygen reduction on disk electrode.

### **3.2.4 MEA Preparation**

A commercially available catalyzed GDE (LT250EW Low Temperature ELAT® GDE Microporous Layer, E-TEK) was used as the anode for the fuel cell test. Cathode catalyst

ink was prepared by thoroughly blending the FeCo-EDA-600R composite catalyst with de-ionized water and recast Nafion ionomer (5% Nafion suspension in alcohols; 1100 Nafion equivalent weight; Solution Technology, Inc.). The catalyst was combined with de-ionized water to achieve a 1:10 ratio by weight. Nafion suspension was added in an amount sufficient to reach a 1:1 volumetric ratio between the ionically-conducting phase (Nafion) and the electronically-conducting phase (catalyst + carbon) in dry cathode catalyst. The mixture was placed in an ice bath to prevent overheating and minimize evaporation of solvents, and then ultrasonically mixed for 100 seconds. A piece of a Nafion 212 membrane was placed on the top of a vacuum table preheated to 80 °C. The vacuum table was used to hold the membrane in place and avoid wrinkling during the catalyst application. Cathode ink was then applied to one side of the membrane using a camel hair brush. Upon completion of the painting, the MEA was left on the heated vacuum table for an additional 30 minutes to allow the cathode catalyst layers to cure. The MEA was then removed from the table and placed in a sealed plastic bag for future use. The cathode catalyst loadings were approximately 4.0 mg/cm<sup>2</sup>.

### **3.2.5 Fuel Cell Measurements**

The MEA was assembled in a 5 cm<sup>2</sup> fuel cell prototype. Hydrophobic double-sided and single-sided carbon-cloth gas diffusion layers “backings” from De Nora USA/E-TEK Inc. were used on the cathode and the anode sides of the MEA, respectively. The MEAs were conditioned in hydrogen-oxygen at 0.40 V and 80 °C. The conditioning was continued until the current density reached a constant level. The flow rates of hydrogen and oxygen were 2

mL/s and 5 mL/s, respectively. The anode and cathode gases were humidified at 90 °C and 80°C, respectively. Back pressures of the H<sub>2</sub>/O<sub>2</sub> during the polarization were set to 30 psi/30 psi, while no back pressures were set for the durability tests.

### **3.3 Results and Discussion**

XRD patterns for the two carbon black supports and FeCo-EDA complex catalysts based on those supports are shown in Figure 10. All samples showed broad carbon peaks at 2-theta = 24.3°. It can be seen that the carbon peak in KJ600 sample is more distinct than that of KJ300. Although the XRD result for FeCo-EDA-300R catalyst shows the evidence of iron and cobalt oxides, the intensity and variety of the peaks representing transition metals in FeCo-EDA-600R are far more distinct. It was hypothesized that even if the same amount of both KJ300 and KJ600 supports are used, the KJ600 support provides much higher surface area to be combined with polymer structure and is able to capture greater amounts of those excess polymer metal composite which KJ300 supports cannot. The graph obtained for FeCo-EDA-600R shows distinct iron and iron oxide peaks (2-theta = 44.7°, 51.9°, 76.4° and 82.3°) and cobalt oxide peaks (2-theta = 32.4°, 48.3°, 64.5° and 73.1°) which verifies the presence of iron and cobalt containing crystalline phase [111].

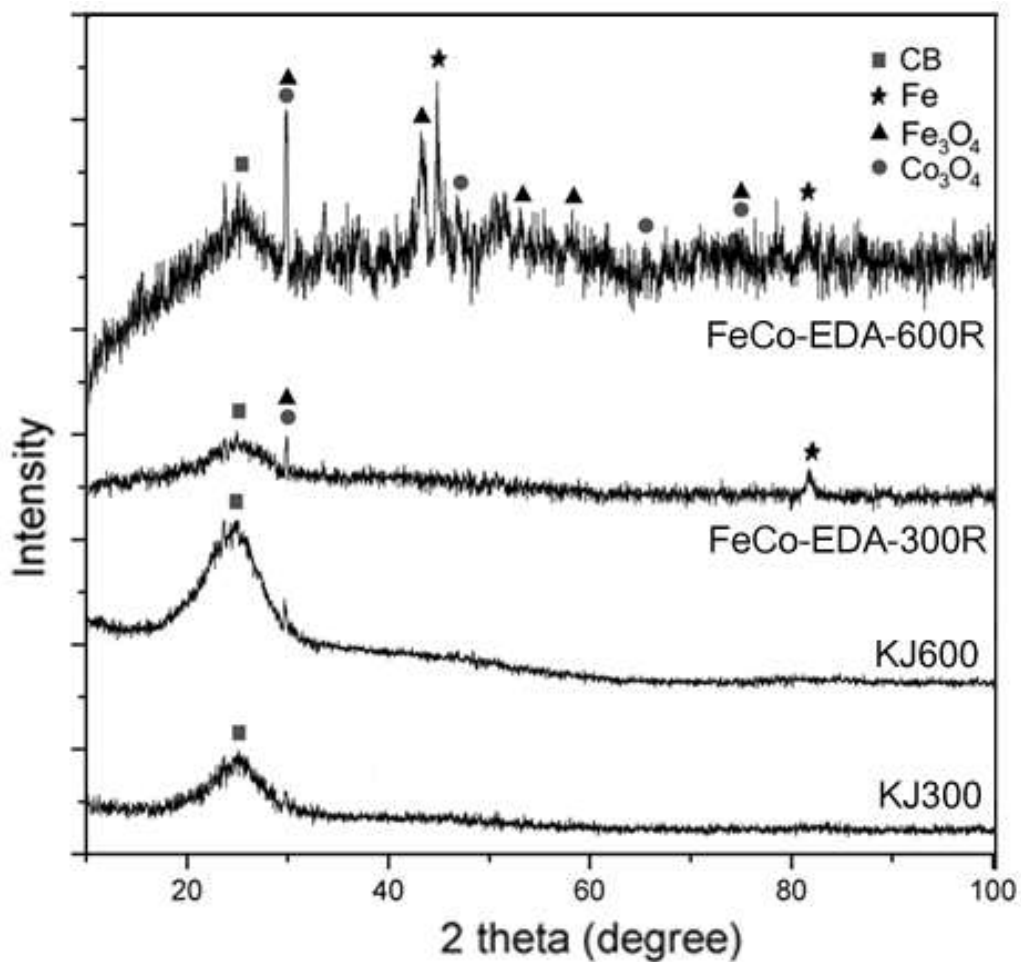


**Figure 10: XRD patterns for functionalized KJ300, KJ600, FeCo-EDA-KJ300R and FeCo-EDA-KJ600R. Reproduced with permissions from [39]. Copyright © 2010 American Chemistry Society**

The elemental analysis carried out by EDX is summarized in Table 2. Both samples contain approximately the same amount of oxygen, but differ in the weight percent of both iron and cobalt. The weight percent of iron and cobalt in FeCo-EDA-600R catalyst is approximately three to four times higher than those of FeCo-EDA-300R, which supports the argument that

the KJ600 support has better capability as a catalyst support to combine with polymer complex due to its larger surface area and pore volume.

**Table 2: EDX elemental analysis of FeCo-EDA-300R and FeCo-EDA-600R samples. Reproduced with permissions from [39]. Copyright © 2010 American Chemistry Society.**

<b>Composition</b>	<b>FeCo-EDA-300R (wt %)</b>	<b>FeCo-EDA-600R (wt %)</b>
Carbon	90.57	83.06
Oxygen	4.73	4.72
Iron	1.43	4.14
Cobalt	1.04	4.31

The electrocatalytic activity of the four catalysts was evaluated using rotating RRDE voltammetry, shown in Figure 12. The half-wave potential and onset potential of each catalyst are summarized in Table 3. The onset potential was measured by taking the potential at which the ORR curves deviated from 0 current from ORR curves corrected for background. This correction was made by obtaining ORR curves at 100, 400, 900 and 1600 rpm in oxygen saturated conditions and subtracting the background current, which was obtained by conducting the voltammetry under nitrogen saturated electrolyte conditions. Similarly, the half-wave potential was measured by finding the potential which was halfway between the limiting current (measured at 0.2 V vs. RHE) and zero current on the ORR

voltammetry curve. The FeCo-EDA-600R shows the best performance, followed by FeCo-EDA-300R, FeCo-EDA-600, and FeCo-EDA-300. From ORR curves, the effect of the refluxing process on the electrocatalytic activity is very clear. Refluxing contributed to the half-wave and onset potential being about 0.25 and 0.15 V higher, respectively. This phenomenon is due to the FeCo-EDA complex effectively allowing the polymerization in full degree, and is deposited in the microporous structure in the carbon support. For both types of samples that have been synthesized without reflux and with reflux, it can also be concluded that the use of KJ600 support improves the catalytic activity of the samples. Compared to KJ300 based catalysts, the half-wave and onset potential of KJ600 based catalysts are shifted to the positive side (average increase of 0.03 and 0.04 V respectively), indicating better electrocatalytic activity due to the increase in the active surface area. ORR curves obtained at various rotating speed for FeCo-EDA-300R and FeCo-EDA-600R are shown in Figure 11.

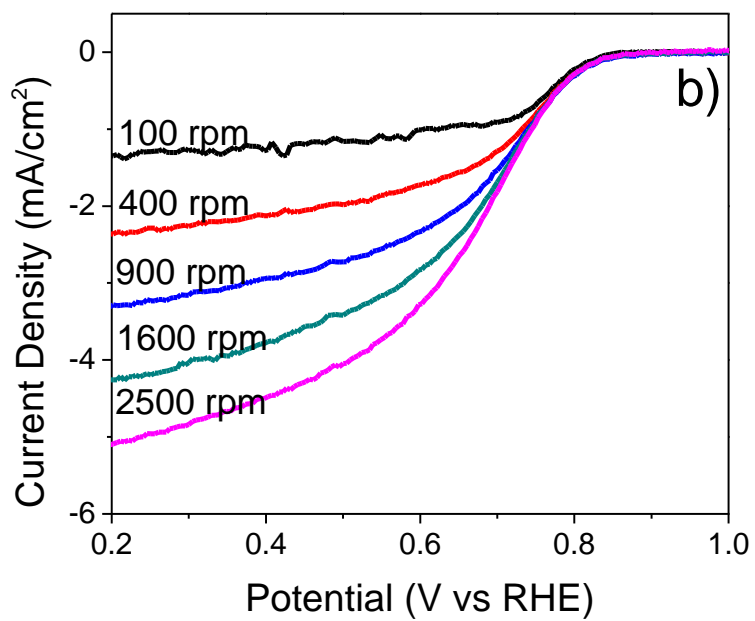
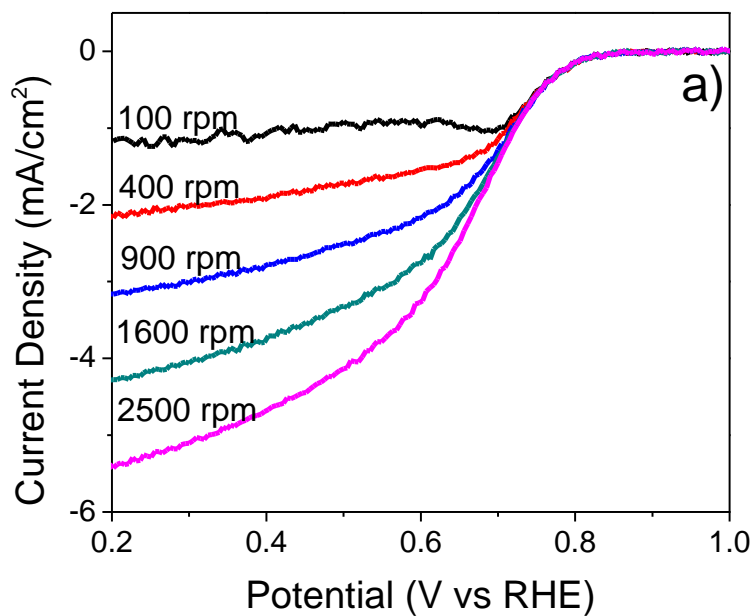


**Figure 11: ORR curves of a) FeCo-EDA-300R and b) FeCo-EDA-600R at various rotation speed in 0.5M H<sub>2</sub>SO<sub>4</sub> electrolyte. Reproduced with permissions from [39]. Copyright © 2010 American Chemistry Society**

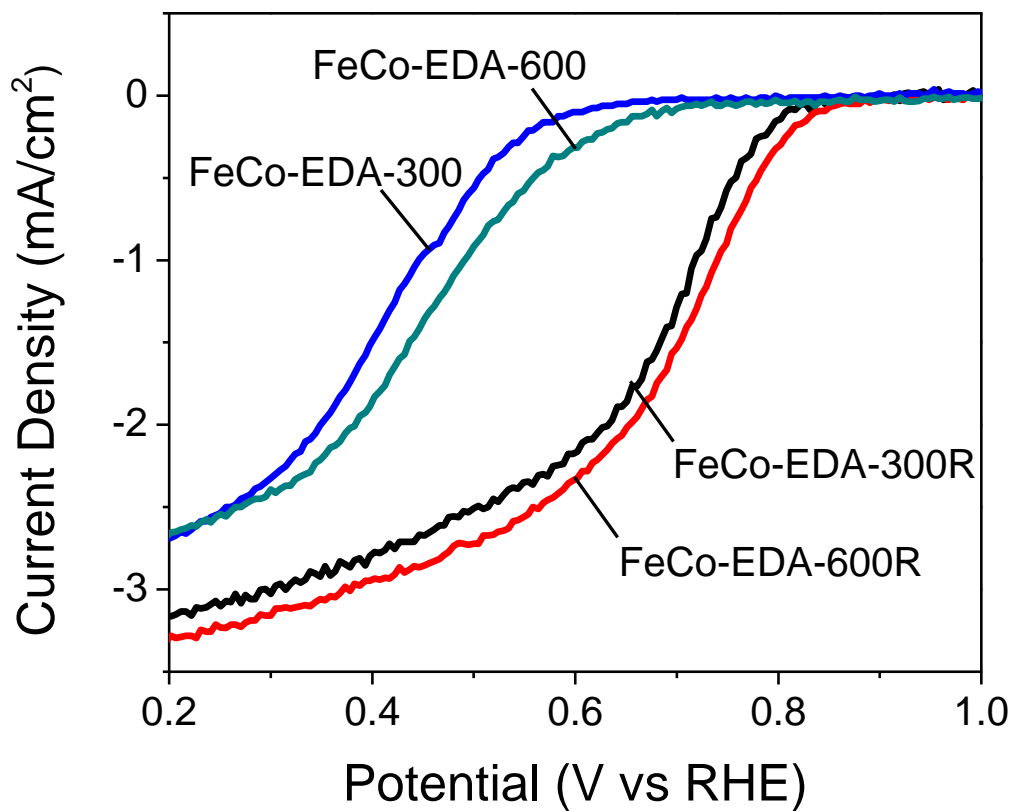
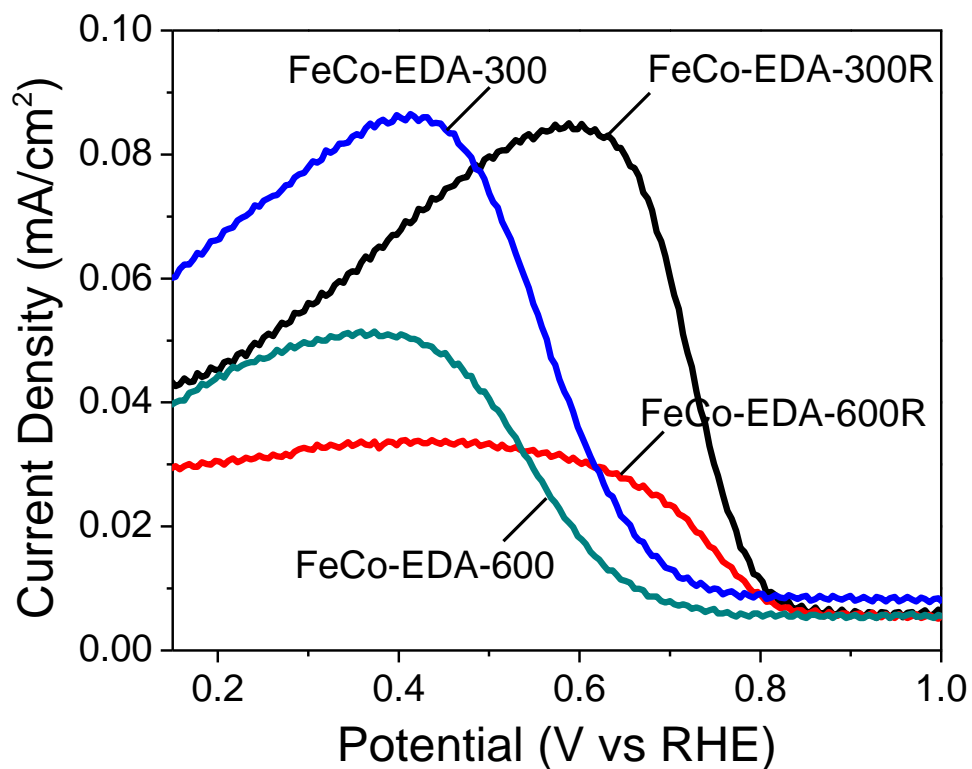


Figure 12: ORR curves of various catalysts; FeCo-EDA-KJ300, FeCo-EDA-KJ600, FeCo-EDA-KJ300R and FeCo-EDA-KJ600R, obtained at 900 rpm in 0.5M H<sub>2</sub>SO<sub>4</sub>. Reproduced with permissions from [39]. Copyright © 2010 American Chemistry Society

**Table 3: Half-wave and onset potential vs. RHE of FeCo-EDA-300, FeCo-EDA-600, FeCo-EDA-300R and FeCo-EDA-600R. Reproduced with permissions from [39]. Copyright © 2010 American Chemistry Society.**

	<b>Half Wave Potential (V)</b>	<b>Onset Potential (V)</b>
FeCo-EDA-300	0.43	0.68
FeCo-EDA-600	0.47	0.73
FeCo-EDA-300R	0.69	0.84
FeCo-EDA-600R	0.72	0.89

The RRDE voltammetry curves showing the amount of hydrogen peroxide generated during ORR process of four samples are illustrated in Figure 13. The current density, which is directly related to the amount of hydrogen peroxide, obtained for KJ300 based catalysts are almost twice that of the KJ600 based catalysts. Between the two KJ600 based ones, FeCo-EDA-600R which showed the best oxygen reduction activity and generated the least amount of hydrogen peroxide during the reaction. The fractional yield of hydrogen peroxide for each sample has been determined and illustrated in Figure 14. The figure shows that KJ300 based catalysts have fractional yield ranging from approximately 10 to 20 percent while the values for KJ600 based catalysts fall in the range of 5 to 10 percent. FeCo-EDA-600R showed the lowest fractional yield of 5 percent. These results indicated that the activity and selectivity of NPMCs could be improved by using higher pore volume and surface area carbon as catalyst support.



**Figure 13: Hydrogen peroxide yield for various catalysts obtained at 900rpm in 0.5M H<sub>2</sub>SO<sub>4</sub>; FeCo-EDA-300, FeCo-EDA-600, FeCo-EDA-300R and FeCo-EDA-600R. Reproduced with permissions from [39]. Copyright © 2010 American Chemistry Society**

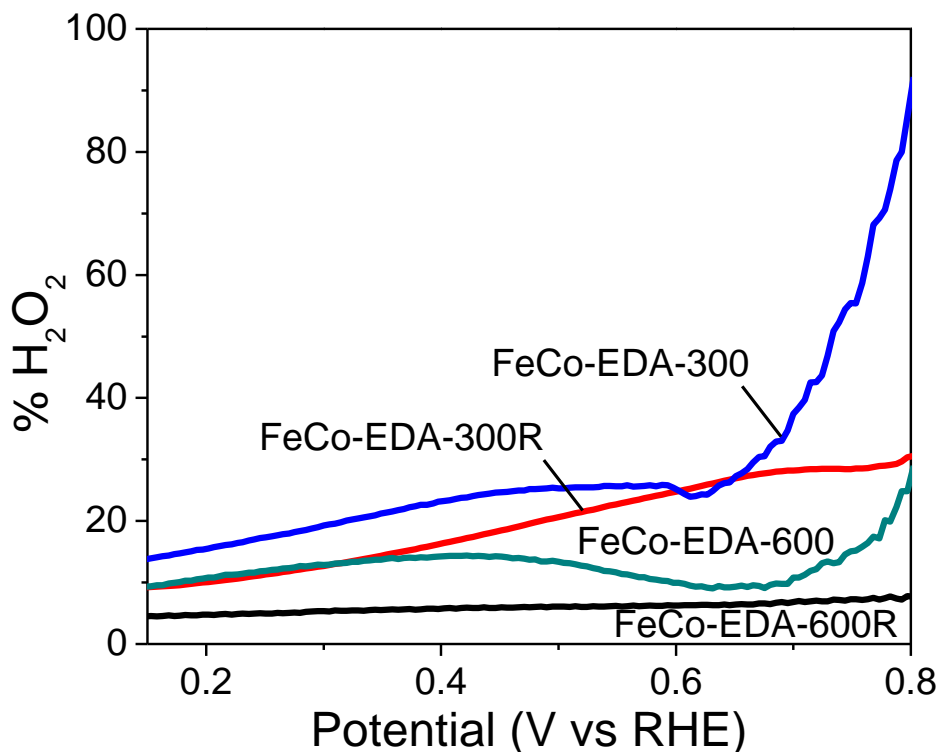


**Figure 14:** The fractional yield of hydrogen peroxide for four samples; FeCo-EDA-KJ300, FeCo-EDA-KJ600, FeCo-EDA-KJ300R and FeCo-EDA-KJ600R. Reproduced with permissions from [39]. Copyright © 2010 American Chemistry Society

The elemental composition and different structural groups of nitrogen in FeCo-EDA-300R and FeCo-EDA-600R were obtained using XPS, shown in Figure 15 and Table 4. From XPS results, FeCo-EDA-600R showed higher nitrogen content (2.15 at.%) compared to FeCo-EDA-300R (1.65 at.%). It is expected that the FeCo-EDA-600R catalyst has higher nitrogen content which could lead to better catalytic activity for various fuel cell catalysts [112].

Further analysis has been carried out on the N 1S signal and the data for all four samples have been plotted in Figure 16. Three distinct peaks are observed, centered at 404.9, 400.7 and 398.3 eV for each catalyst. The peaks at 404.9 and 398.3 eV are known as pyridinic N<sup>+</sup>-O<sup>-</sup> and pyridinic nitrogen groups respectively, while there is some uncertainty regarding the peak at 400.7 eV since it is close to both the peak of pyrrolic nitrogen group at 400.5 eV and the peak of quaternary nitrogen group at 401.3 eV. In this report, the middle peak will be considered as the co-existence of both pyrrolic and quaternary nitrogen groups. The graph clearly shows that for FeCo-EDA catalyst, the amount of nitrogen content (which can be determined by calculating the area under the curves) is directly related to the electrocatalytic performance. Although the contribution to the catalytic activity of the pyridinic N<sup>+</sup>-O<sup>-</sup> nitrogen groups seems ambiguous, it is hypothesized that pyrrolic/quaternary and pyridinic peaks lead to formation of complex structures that are better suited as catalysts. From the Figure 16, it can be observed that the amplitude of the pyridinic peak is rising as the catalyst performance is increased, compared to the other nitrogen peaks. It has been studied that the formation of pyridinic nitrogen groups is observed on the edge of the graphite plane and the lone pair of electrons from pyridinic nitrogen groups has been attributed to be ORR active [113]. The higher exposure of the planar edges of graphite in FeCo-EDA-600R due to the more rugged surface structure is expected to expose more pyridinic nitrogen which enhances ORR activity. For these reasons it is expected that ORR activity of FeCo-EDA-600R be greatest.

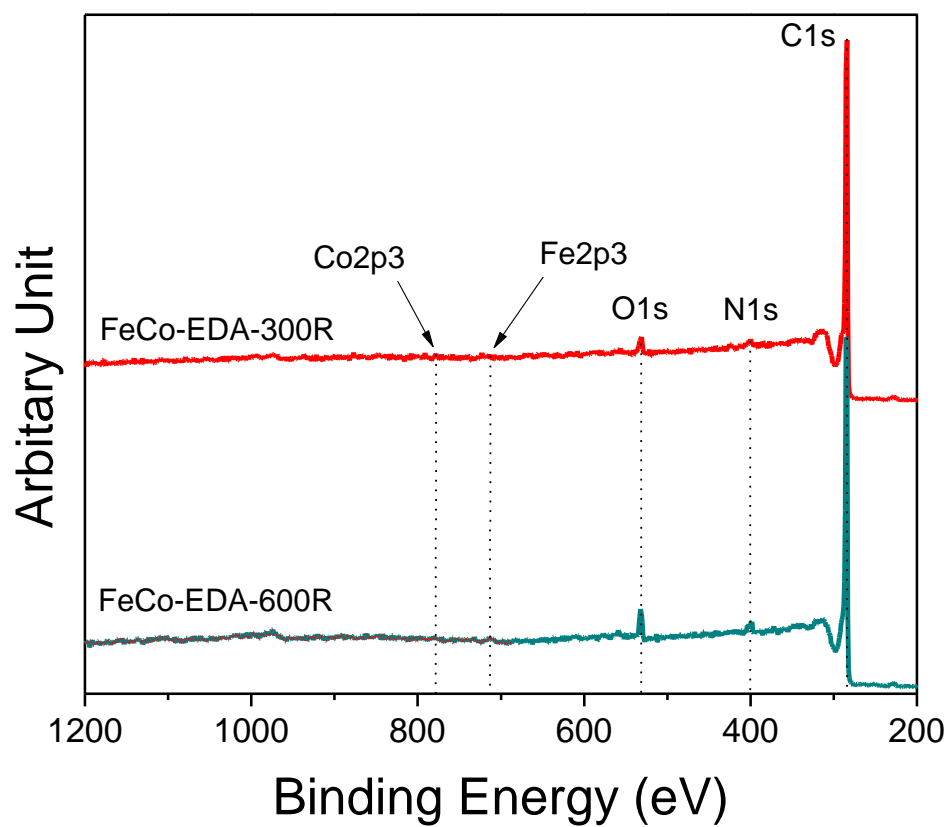


**Figure 15: XPS spectrum of FeCo-EDA-KJ300R and FeCo-EDA-KJ600R showing all the elements in the samples. Reproduced with permissions from [39]. Copyright © 2010 American Chemistry Society**

**Table 4: XPS analysis of the elemental composition of FeCo-EDA-300R and FeCo-EDA-600R.**

Reproduced with permissions from [39]. Copyright © 2010 American Chemistry Society.

	FeCo-EDA-300R		FeCo-EDA-600R	
	Peak Position (eV)	At. %	Peak Position (eV)	At. %
<b>Carbon</b>	~284.36	96.25	~284.48	94.33
<b>Nitrogen</b>	~400.01	1.66	~400.74	2.18
<b>Oxygen</b>	~531.24	2.09	~532.13	3.49

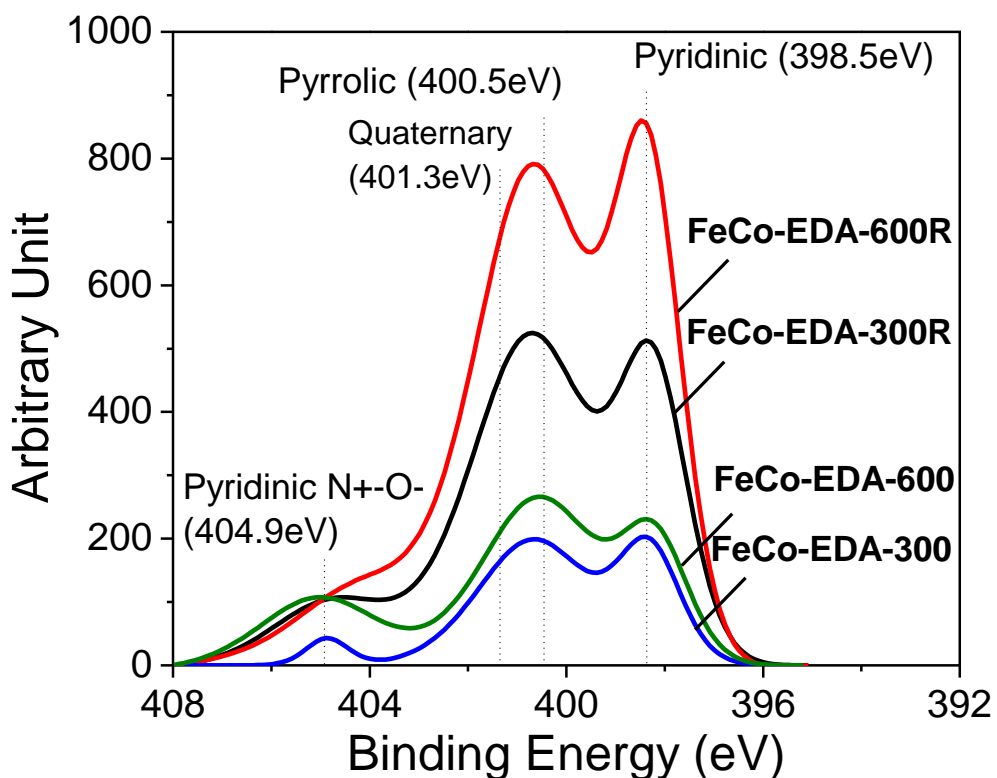


**Figure 16: XPS spectrum showing the presence of different types of nitrogen groups from the N 1s signal. Reproduced with permissions from [39]. Copyright © 2010 American Chemistry Society**

In order to evaluate ORR catalytic activity of the FeCo-EDA-600R catalyst in practical fuel cell applications, an MEA was fabricated with the catalyst at the cathode and tested using a fuel cell test station. The PEM fuel cell polarization curve was obtained at 80 °C using 30 psi back pressure for both H<sub>2</sub> and O<sub>2</sub>. The polarization curves and the corresponding power density curves are shown in Figure 17. At a cell voltage of 0.6 V the current density is 0.37 A/cm<sup>2</sup> with a maximum power density of 0.44 W/cm<sup>2</sup>. The stability of the FeCo-EDA-600R catalyst material was tested by holding the cell voltage at 0.4 V at 80 °C for 100 hours. No back pressure was applied to the MEA and the cathode catalyst loading was 4.0 mg/cm<sup>2</sup>. Figure 18 graphically depicts this current transient for the H<sub>2</sub>/O<sub>2</sub> cell with no visible degradation in performance.

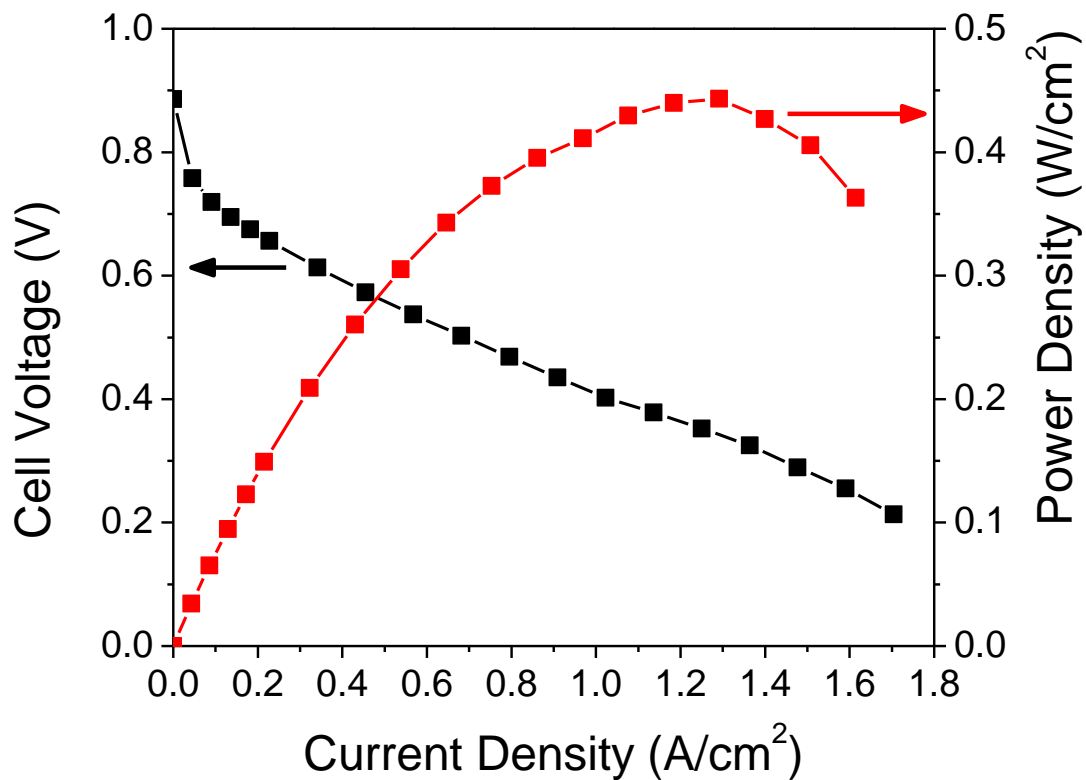


**Figure 17: Polarization curve and corresponding power densities of MEAs fabricated with FeCo-EDA-KJ600R cathode catalyst and commercially available catalyzed GDE anode. Cell temperature: 80°C; Catalyst loading: 4 mg/cm<sup>2</sup>; H<sub>2</sub>/O<sub>2</sub> back pressures: 30 psi/30 psi. Reproduced with permissions from [39]. Copyright © 2010 American Chemistry Society**

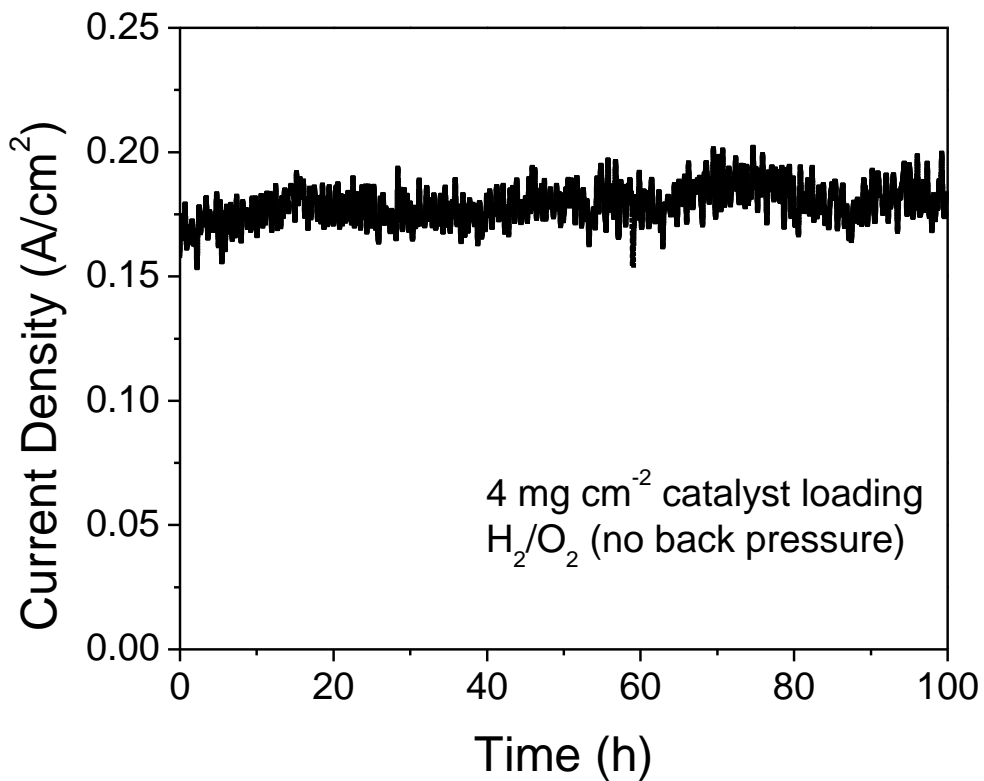


**Figure 18: Durability test of the H<sub>2</sub>/O<sub>2</sub> PEM fuel cell at 0.4V for 100 hours. MEA was fabricated with FeCo-EDA-KJ600R catalyst and commercially available catalyzed GDE as the cathode and anode respectively. Cathode catalyst loading: 4 mg/cm<sup>2</sup>; Cell temperature: 80°C; No back pressure. Reproduced with permissions from [39]. Copyright © 2010 American Chemistry Society**

### **3.4 Conclusions**

Non-precious metal catalysts were developed by in-situ polymerization of ethylenediamine with iron and cobalt on two different porous carbon black supports in order to improve ORR

activity. Among those materials, the FeCo-EDA-600R catalyst possesses the highest electrochemical activity for ORR, as well as the least amount of hydrogen peroxide generated at approximately 5 percent. Between the two carbon graphite catalyst support, KJ300 and KJ600, KJ600 showed greater potential in generating higher catalytic activity when used as a non-precious metal catalyst due to its higher pore volume and surface area. During synthesis, KJ600 leads to higher nitrogen content providing more active sites for ORR. When non-precious metal catalyst is synthesized using this in-situ method, given enough time for the polymerization to happen in full degree is a critical parameter which leads to noticeable improvements in ORR performance. The MEA fabricated with the FeCo-EDA-KJ600R catalyst maintained high power densities. At a cell voltage of 0.3V a current density of  $1.4 \text{ A/cm}^2$  was achieved with a maximum power density of  $0.44 \text{ W/cm}^2$ . Further study will be necessary to determine the durability of the MEA in fuel cell operating conditions. However, it can be concluded that higher pore volume and surface area of carbon support could lead to higher nitrogen content providing more active sites for ORR and this type of catalyst has great potential used as a non-precious PEM fuel cell catalyst.

## **Section 4: Graphene Nanosheets Supported Non-precious Catalyst**

### **4.1 Introduction and Motivation**

While platinum is the most commonly used catalyst material for the oxygen reduction reaction occurring at the cathode of polymer electrolyte membrane fuel cells (PEMFCs), the high cost and limited natural abundance of this noble metal still limits the large-scale commercialization of this technology [63, 114]. As a substitute for platinum, the development of non-precious metal catalysts (NPMCs) with high ORR activity and practical durability has been viewed as the long-term solution to reduce the overall cost of PEMFC systems [24, 44, 115]. Despite ample investigations being done with steady progress realized in this field, the performance of even the best NPMCs is still inferior to that of precious metal catalysts and thus it is a stringent necessity to develop alternative preparation strategies to improve the ORR activity and the durability of NPMCs [22, 26, 116]. Utilization of carbon support materials with unique structural and physical properties has been demonstrated as a feasible method to tailor the catalytic activity and the stability of NPMC composites [117], owing to the specific catalyst-support interactions and favourable carbon support properties including porosity, high surface areas, electronic conductivity and electrochemical stability. Specifically, significant efforts have been devoted to the utilization of novel nanostructured carbon supports with large surface areas and pore volumes, including carbon nanotubes [61], carbon nanofibers [25], and mesoporous carbons [39].

Despite promising performance achieved in terms of ORR activity using these nanostructured support materials, there is still enormous demand and potential for NPMC improvement, especially in durability.

Graphene, consisting of a two-dimensional (2D) monolayer of graphitic carbon atoms, has been viewed as a promising candidate for the fuel cell catalyst support, due to its many intriguing properties such as high aspect ratios, large surface areas, rich electronic states, good electron transport, thermal/chemical stability and good mechanical properties [118, 119]. Scientists have already developed graphene based metal-free fuel cell catalysts showing better ORR activity and durability than the commercial Pt/C catalyst in alkaline condition [119-121], however, despite the immense promise of these materials, the application of graphene as a NPMC support remains essentially unexplored, especially in acidic electrolyte conditions. In the present study, we report the development of a novel NPMC in acid electrolyte using pyrimidine-2,4,5,6-tetramine sulfuric acid hydrate (PTAm) as a nitrogen precursor and graphene nanosheets as catalyst supports. We investigate the effect of different pyrolysis temperatures on the catalysts' ORR activity along with detailed surface analysis to provide insight regarding the nature of the ORR active surface moieties. This novel NPMC demonstrates promising electrocatalyst activity and durability superior to that of commercial catalyst for the ORR, rendering graphene nanosheets as a suitable replacement to traditional nanostructured carbon support materials.

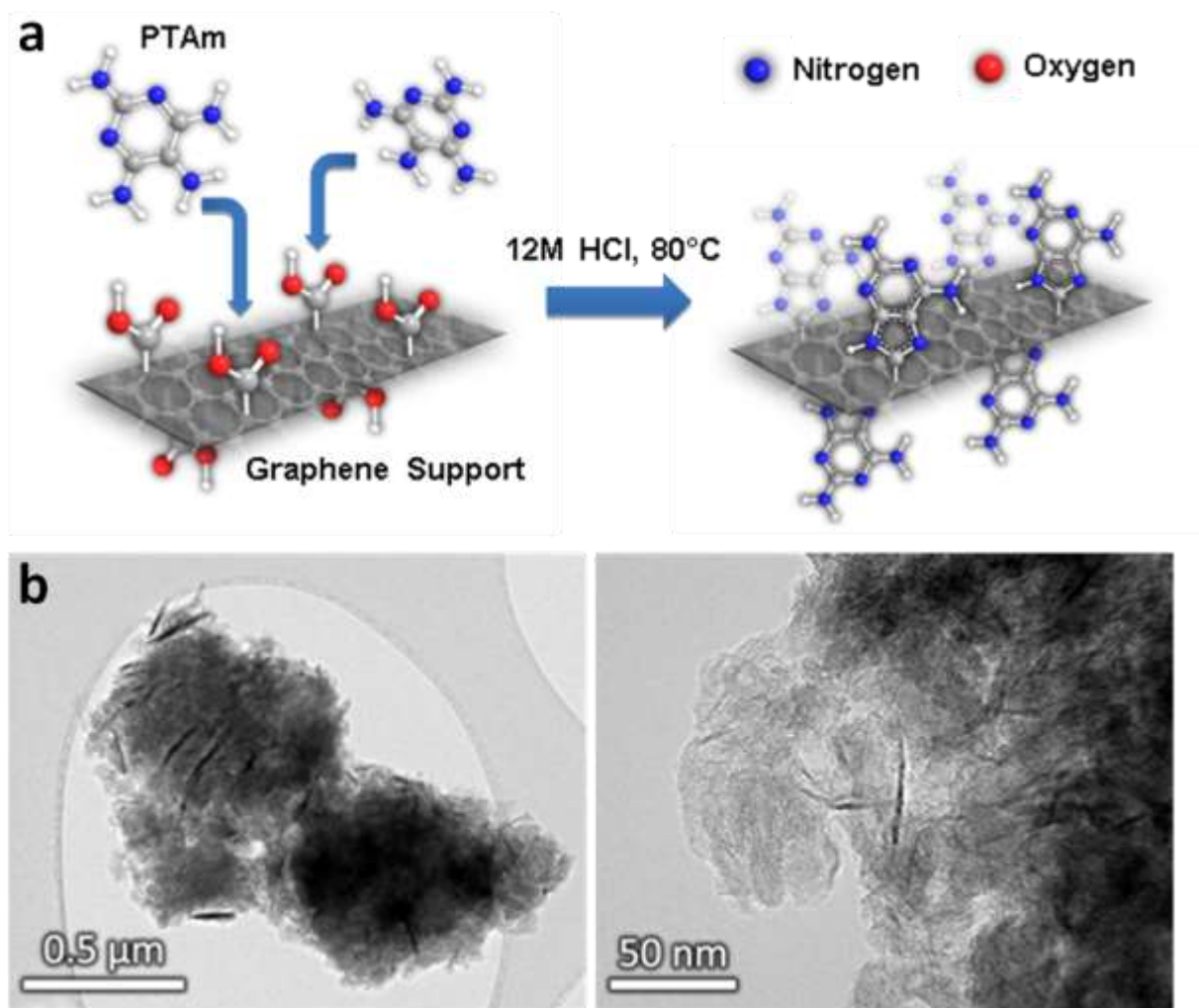


Figure 19: (a) Proposed schematic representation of the coupling reaction of pyrimidine-2,4,5,6-tetramine sulfuric acid hydrate to graphene nanosheets. (b) Two TEM images of Fe-PTAm/Graphene pyrolyzed at 800°C, obtained at different magnifications. Reproduced with permissions from [122]. Copyright © 2011 ECS – The Electrochemical Society

## **4.2 Experimental**

### **4.2.1 Synthesis of Fe-PTAm/G**

To prepare graphene nanosheet supported NPMCs using PTAm as a nitrogen precursor and iron acetate (FeAc) as a metal precursor, a desired amount of graphene and PTAm was added to 4M HCl solution, and the solution was subjected to low temperature heat treatment at 80 °C for 24 h while stirring. The proposed coupling reaction between the support and PTAm is illustrated in Figure 19a [123]. The mixture was filtered, washed with deionized water and dried overnight in an oven at 60 °C. The dried sample was then ground to a fine powder and ultrasonically mixed with 1 wt. % FeAc in 50 mL of ethanol for one hour. The solution was again filtered and dried in an oven. The remaining dried precipitate was pyrolyzed at various temperatures ranging from 700 to 1000 °C for one hour under nitrogen gas flow. These catalysts are referred as FPGNP (non-pyrolyzed), FPG700, FPG800, FPG900 and FPG1000 accordingly.

### **4.2.2 Physical Characterization**

All samples were analyzed by XRD, SEM, XPS, and NAA. XRD analysis was done with an Inel XRG 3000 diffractometer using a Cu-K $\alpha$  source. A broad range scan of the 2 $\theta$  range from 0.288° to 113° was captured for about 10 minutes per sample. A LEO FESEM 1530 was used to take SEM images at 100 kx magnification at 20 kV. XPS was carried out using a Thermal Scientific K-Alpha XPS spectrometer at 150 eV to investigate the relative content of different elements and the relative content of different types of nitrogen bondings. BET

surface areas and pore size distributions were obtained through N<sub>2</sub> adsorption/desorption isotherms using an Autosorb 1 from Quantachrome. Prior to N<sub>2</sub> adsorption/desorption, samples were subject to an outgassing pretreatment by heating the sample at 100°C in a vacuum overnight.

#### **4.2.3 Rotating Ring Disc Electrode Experiments**

The electrocatalytic activity was evaluated in a three-electrode electrochemical cell using a Pine-Instrument's Bipotentiostat AFCBP1, equipped with a speed rotator. All RDE measurements were performed in acidic 0.1M HClO<sub>4</sub> electrolyte at room temperature, using a Ag/AgCl reference electrode. To prepare the glassy carbon working electrode (0.19635 cm<sup>2</sup>), 4 mg of catalyst sample was ultrasonically dispersed in 1 mL of ethanol. 30 μL of the ink and 5 μL of 0.5 wt. % Nafion solution were applied to the glassy carbon disk, leading to identical electrode catalyst loadings for each sample during testing. ORR curves were recorded at a scan rate of 10 mV/s with the electrolyte saturated with oxygen gas under various electrode rotation speeds (100, 400, 900 and 1600 rpm). ORR curves were corrected by removing background currents obtained under the same testing conditions in nitrogen saturated electrolyte. Transmission electron microscopy (TEM) was utilized to observe the surface morphology, and X-ray photoelectron spectroscopy (XPS) was conducted to determine surface atomic compositions and configurations.

### 4.3 Results and Discussion

The morphology of FPG800 observed by TEM is displayed in Figure 19b. Many small graphene nanoplatelets were observed clustered together, possibly resulting from the linkage between PTAm molecules and adjacent graphene sheets, since PTAm contains many nitrogen sites that can be coupled to the edge plane of the graphene and the functional groups [123]. These adjacent graphene nanosheet clusters can serve to host one of the most promising metal-nitrogen active sites structures upon pyrolysis [21].

Half-cell RRDE experiments were conducted for all samples to determine their catalytic activity for the ORR, with polarization curves plotted in Figure 20a at a rotation rate of 900rpm. From these results, it is clear that a pyrolysis step is crucial, where FPGNP demonstrated negligible ORR activity. FPG800 displayed optimal activity, demonstrating an onset potential of 0.853 V and a half-wave potential of 0.692 V (vs. RHE) and full RRDE data at various rotation rates provided in Figure 20b. At pyrolysis temperatures above or below 800°C reduced onset potentials and current densities were observed.

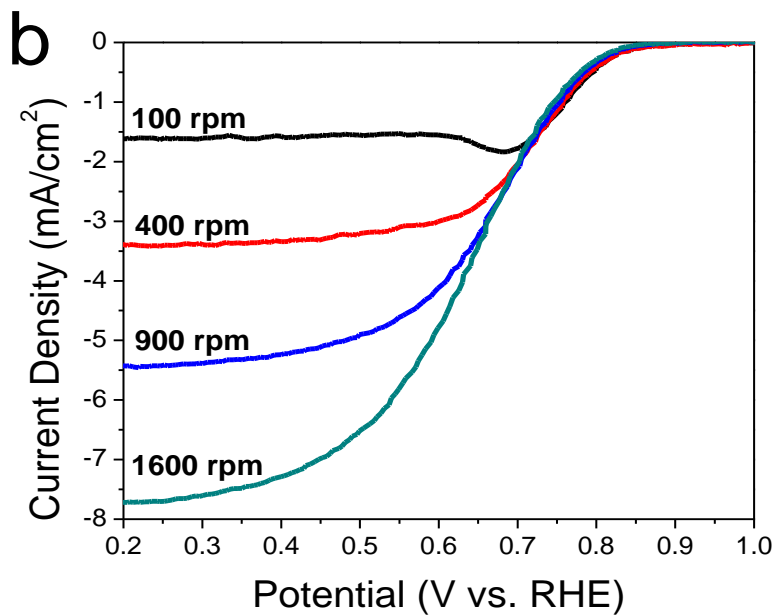
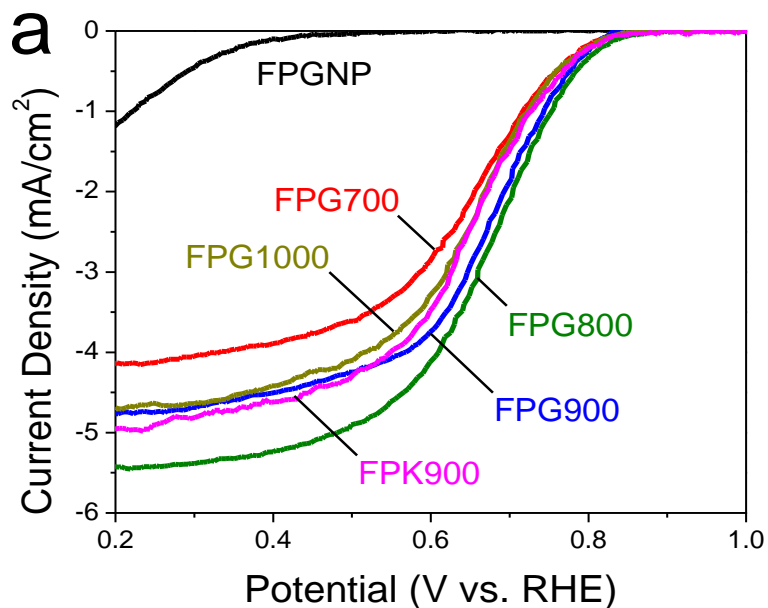


**Figure 20:** (a) ORR curves of Fe-PTAm/Graphene catalysts heat-treated in  $N_2$  using different pyrolysis temperatures, obtained at 900 rpm. (b) ORR curves of FPG800 at various rotation speeds. Reproduced with permissions from [122]. Copyright © 2011 ECS – The Electrochemical Society

Moreover, the H<sub>2</sub>O selectivity of these samples was determined from ring current data, with high selectivity values providing indication of a more efficient 4 electron reduction pathway compared to the inefficient 2 electron reduction forming destructive H<sub>2</sub>O<sub>2</sub> species. Figure 21 provides H<sub>2</sub>O selectivity of all four pyrolyzed graphene based catalysts with the order of highest to lowest H<sub>2</sub>O selectivities being FPG800 > FPG900 > FPG 1000 and FPG700, consistent with ORR activity results. Specifically, FPG800 shows the best H<sub>2</sub>O selectivity of 99.9% at 0.4 V vs. RHE, indicating negligible selectivity towards the two electron reduction pathway. The results of the onset potentials, current densities obtained at 0.6V vs. RHE and H<sub>2</sub>O selectivities are tabulated in Table 5 for all synthesized catalysts.

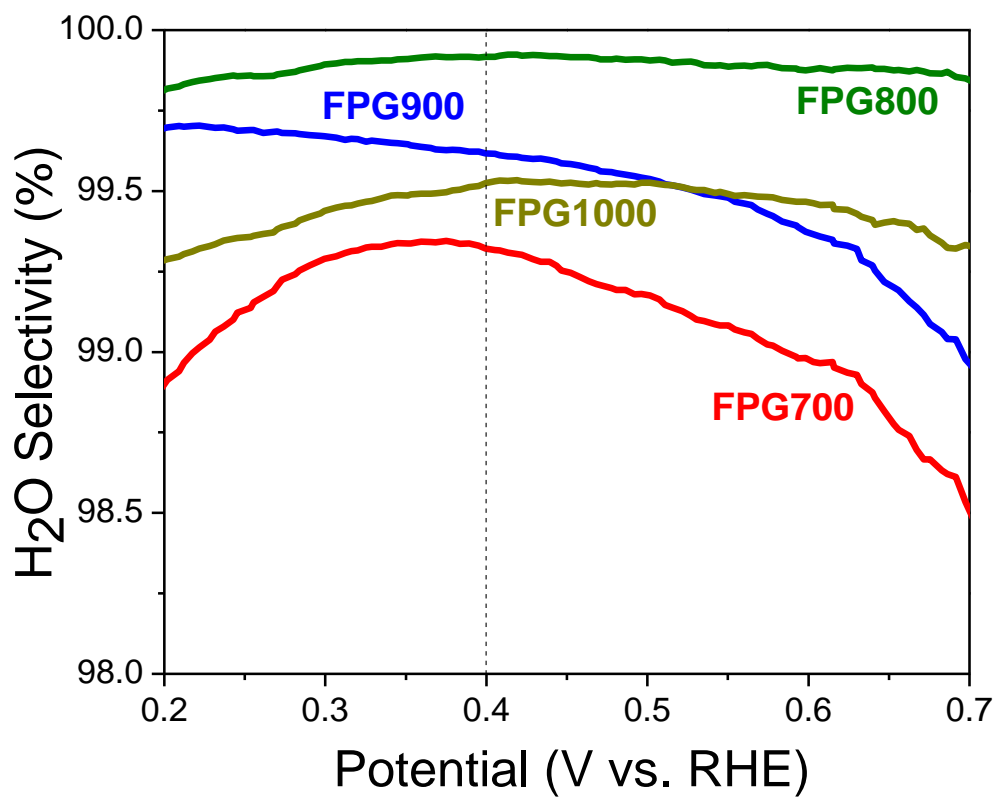


**Figure 21:** H<sub>2</sub>O selectivity for the Fe-PTAm/Graphene catalysts, obtained at 900 rpm. Reproduced with permissions from [122]. Copyright © 2011 ECS – The Electrochemical Society

**Table 5: Summary of RRDE experiments for synthesized catalyst samples. Reproduced with permissions from [122]. Copyright © 2011 ECS – The Electrochemical Society**

	Current Density at 0.6 V vs. RHE (mA/cm <sup>2</sup> )	Onset Potential (V vs. RHE)	H <sub>2</sub> O (V at 0.4 V vs. RHE (%))	Selectivity
FPGNP	0.01	0.446		
FPG700	2.88	0.839		99.3
FPG800	4.12	0.853		99.9
FPG900	3.75	0.845		99.6
FPG1000	3.32	0.836		99.5
FPK900	3.49	0.838		

To evaluate the effect of utilizing graphene as the NPMC support, the same type of catalyst was fabricated using Ketjen 600JD carbon black support. This porous carbon has been previously established as a good electrocatalyst support and thus serves as a good performance evaluation benchmark. Catalyst synthesis conditions were identical with the NPMC, with the exception of the carbon support material utilized. Pyrolysis was carried out at the same temperatures as well; however, the activity of only the highest performing material pyrolyzed at 900°C is illustrated in Figure 20a. From the presented curves, it can clearly be seen that the ORR performance of the graphene based catalysts exceeds that of the ketjen black based catalyst for this type of catalyst, which effectively demonstrates the promising potential for the graphene as a catalyst support.

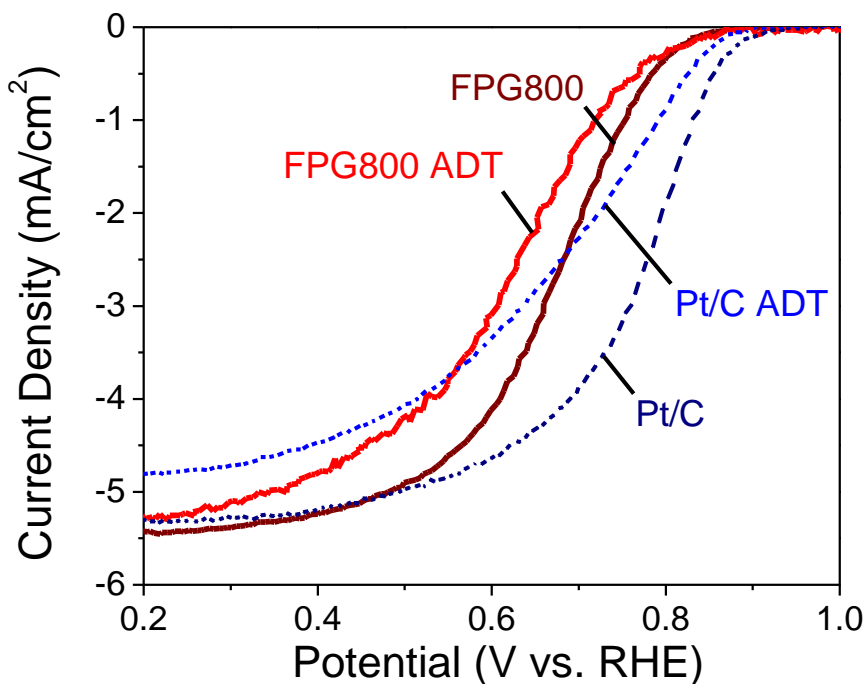


**Figure 22: ORR curves of FPG800 before and after running 1000 CV cycles in nitrogen saturated electrolyte. Reproduced with permissions from [122]. Copyright © 2011 ECS – The Electrochemical Society**

The durability of FPG800 was investigated by accelerated degradation testing (ADT) consisting of 1000 cycles in N<sub>2</sub> saturated electrolyte at a scan rate of 50 mV/s between 0 and 1.2 V vs. RHE. Durability data is provided in Figure 22 along with commercial carbon supported platinum (Pt/C) for comparison. Surprisingly, FPG800 showed only a slight decrease of 0.055 V in the half-wave potential while Pt/C showed a much higher potential decrease of 0.125 V. Moreover, the current densities obtained at 0.2 V vs. RHE before and after the cycles for FPG800 showed almost no difference (0.016 mA/cm<sup>2</sup>) while the

difference for Pt/C was 0.055 mA/cm<sup>2</sup>. The resulting current density at 0.2 V vs. RHE for FPG800 following ADT was approximately 10 % higher than that of the commercial catalyst. Overall, FPG800 showed superior durability than that of the commercial carbon supported platinum catalyst under the studied conditions. This provides indication of the promising stability of these materials most likely arising due to the high graphitic content [120].

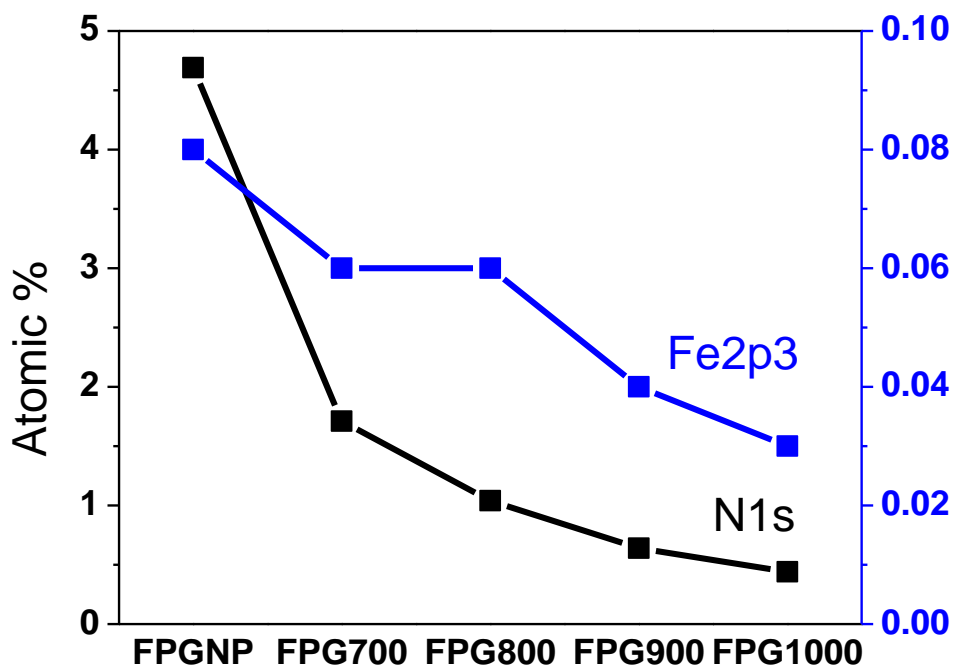


**Figure 23: XPS summary of surface atomic composition of Fe-PTAm/Graphene catalysts. Reproduced with permissions from [122]. Copyright © 2011 ECS – The Electrochemical Society**

XPS was utilized to determine the surface atomic composition and chemistry of the catalyst samples. XPS confirmed the presence of a variety of carbon, and nitrogen species, along with trace amounts of iron as illustrated in Figure 23. A decreasing trend was observed for the surface nitrogen content with increasing pyrolysis temperatures, consistent with previous reports indicating decomposition of nitrogen species at elevated temperatures [45]. High resolution N1s spectra along with a detailed breakdown of the contributing species obtained after peak de-convolution are provided in Figure 24 and 25, respectively. It should be noted that the scale for the intensity obtained for each catalyst has been adjusted for better visibility. Specifically, the N1s spectra was broken down into three peaks representing pyridinic (398.3 eV), pyrrolic (400.5 ~ 401 eV), and quaternary (401 ~ 403 eV) nitrogen functionalities [124]. Following pyrolysis at 700°C, the relative amount of pyridinic nitrogen increased to 59.41 at.% of all the nitrogen groups, and dropped slightly to 54.79 at.% for the sample pyrolyzed at 800°C [37]. By further increasing the final pyrolysis temperature, the relative amount of pyridinic nitrogen decreases, as these species are relatively unstable at temperatures exceeding 800°C. The slight decrease in the relative amount of pyridinic nitrogen from 700 to 800°C, combined with a stable iron surface content observed from 700 to 800°C despite significant changes in the observed ORR activity can possibly indicate specific active site formation, or a transition of the active site from FeN<sub>4</sub>/C to FeN<sub>2+2</sub>/C structures. It has been reported that, while FeN<sub>4</sub>/C is the most prominent active site at lower pyrolysis temperatures FeN<sub>2+2</sub>/C catalytically active sites arise in the range of 700 to 800°C and reach the highest concentration at 800°C [125]. It has also been reported previously for catalysts using FeAc as the iron precursor and with low iron content (less than 0.2 wt %),

FeN<sub>2+2</sub>/C active sites dominate the catalytic behaviour, while forming better electrical contact with the conductive graphene plane [125, 126]. Moreover, as it can be seen in Figure 25 the relative amount of pyrrolic and quaternary nitrogen increases with increased pyrolysis temperature, as these forms of nitrogen are stable at higher temperatures [125]. Thus, for this particular NPMC, there is no correlation between these two nitrogen groups and the performance. Thus, the catalyst performance reaches the highest at the temperature of 800°C and drops with increasing temperature due to both FeN<sub>2+2</sub>/C active site and the overall nitrogen content decrease.

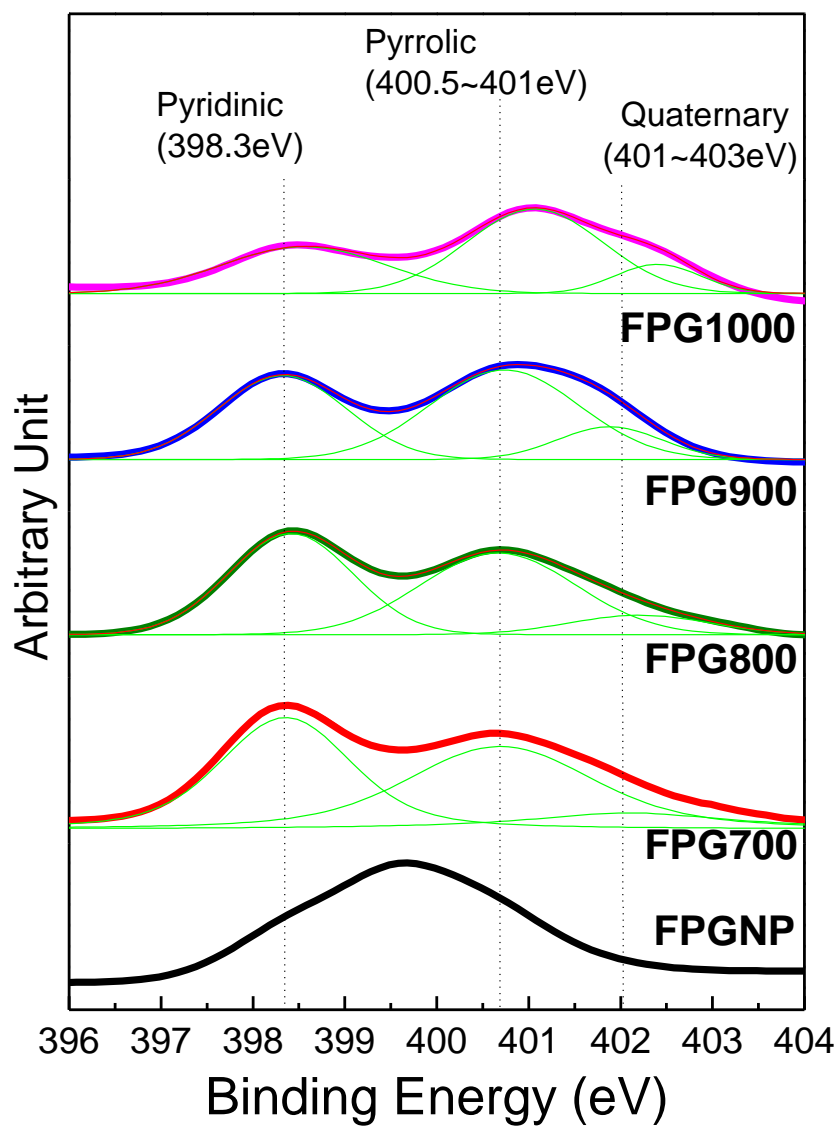


**Figure 24:** N 1s narrow scan spectra of the various FPG samples. Reproduced with permissions from [122]. Copyright © 2011 ECS – The Electrochemical Society

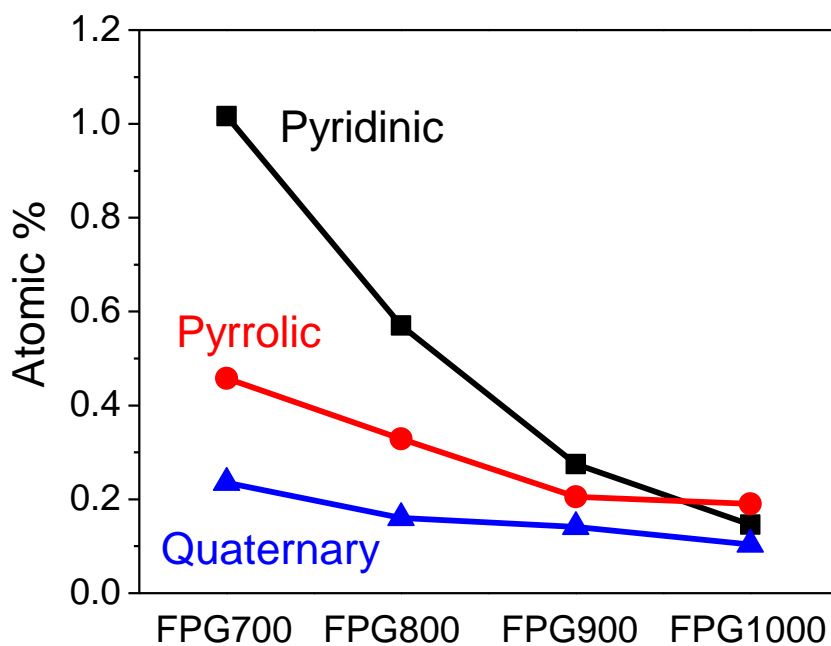


**Figure 25: Nitrogen content of the various FPG samples. Reproduced with permissions from [122]. Copyright © 2011 ECS – The Electrochemical Society**

#### 4.4 Conclusions

We have successfully synthesized a novel NPMC using PTAm as a nitrogen precursor, FeAc as iron precursor and graphene nanosheets as a catalyst support. This NPMC demonstrates promising electrocatalytic activity and durability for the ORR, rendering graphene nanosheets as a suitable replacement to traditional nanostructured carbon support materials. A pyrolysis procedure was deemed crucial for active site formation, where the NPMC sample heat treated at 800°C was found to display optimal ORR activity and H<sub>2</sub>O selectivity, specifically, an onset potential of 0.853 V vs RHE, a half-wave potential of

0.682 V vs RHE, and a H<sub>2</sub>O selectivity of ca. 99.9 %. Moreover, high stability through ADT was demonstrated most likely due to the high graphitic content of the catalyst support material. Thus, graphene nanosheets are presented as an ideal catalyst support material, with promising ORR activity and stability demonstrated. Future investigations will focus on catalyst optimization by varying iron precursor loading and synthesis conditions, which have previously been deemed important factors influencing the ORR activity.

## **Section 5: Nitrogen-doped Activated Graphene Supported Platinum Electrocatalyst**

### **5.1 Introduction and Motivation**

The material on which the catalyst is supported is important for the high dispersion and narrow distribution of Pt nanoparticles, and these characteristics are closely related to electrocatalytic activity of the catalysts[64]. The support materials can influence the catalytic activity by interplaying with catalytic metals, and the durability of the catalyst is also greatly dependent on its support[70]. A variety of support materials like carbons, oxides, carbides, and nitrides have been employed as supports materials for Pt[71-76], and much effort has been devoted to the synthesis of the novel carbon supports with large surface area and pore volume, including nanostructured carbons such as carbon nanotubes (CNTs), carbon nanofibers, and mesoporous carbon[25, 39, 61, 65, 67, 77, 78]. For example, nanostructured carbon supported Pt catalysts have shown improved catalytic activity and durability compared to the commercial catalyst supported on Vulcan XC-72 carbon black, due to the structural and electrical properties of CNTs[66]. Mesoporous carbon supported Pt catalysts also have shown excellent performance in PEM fuel cell electrode reactions, attributed to the high uniform dispersion of catalytic metals, the high electrical conductivity, and the enhanced mass transfer due to the pore structure of the materials[58, 60]. The carbon support can also be doped by other atoms or compounds in order to obtain both improved catalytic activity and enhanced durability for ORR[62, 79, 80]. These novel nanostructured

carbon materials have achieved promising performance in terms of catalytic activity and durability. However, there is still enormous demand and potential for the catalysts to improve.

Graphene, consisting of a two-dimensional (2D) monolayer of graphitic carbon atoms, has been viewed as a promising candidate for the fuel cell catalyst support, due to its many intriguing properties such as high aspect ratios, large surface areas, rich electronic states, good electron transport, thermal/chemical stability and good mechanical properties [118, 119]. Especially nitrogen-doped graphene has been found to have an excellent electrochemical activity towards ORR even though the real active site and the reaction mechanism of nitrogen-doped species with oxygen are still unclear [127]. In this study, we have developed Pt catalyst by combining the precious metal with nitrogen-doped activated graphene (N-AG) as the support. A transmission electron microscopy (TEM) image of the catalyst in Figure 27 shows uniform size and distribution of platinum nanoparticles on a graphene layer. This novel catalyst demonstrates superior electrocatalyst activity and durability over Pt/XC72 catalyst for ORR under the studied conditions, rendering graphene as an ideal replacement to traditional nanostructured carbon support materials.

## **5.2 Experimental**

### **5.2.1 Activated Graphene Synthesis**

The activated graphene (AG) and nitrogen-doped activated graphene (N-AG) was synthesized by thermal shock method [128]. Graphene oxide undergoes thermal shock from room temperature to 800°C within five seconds in inert atmosphere in a tube furnace. It has

been studied that by rapidly raising the temperature, it maximizes the exfoliation of the GO sheets due to higher diffusion rate of the evolved gases during the decomposition of the oxygen groups in GO than the van der Waals forces holding the GO sheets together. The exfoliated graphene is then soaked in 7 M KOH for 24 hours and filtered, followed by drying in an oven. The powder is once again heated at 900 °C in the tube furnace in inert atmosphere to synthesize activated graphene. Lastly, another heat treatment in the presence of ammonia gas completes the synthesis of nitrogen-doped activated graphene. The activated sample undergoes a rapid heating from room temperature to 800 °C by sliding a long quartz tube containing the sample in the tube furnace and was kept for an hour before it cools down. The nitrogen-doping of exfoliated graphene happens in the presence of ammonia (1:1 ratio of ammonia and argon, each at 50 sccm), which reacts with oxygen groups in GO to form C-N bonds. The schematic representation of activated graphene support synthesis is illustrated in Figure 26.

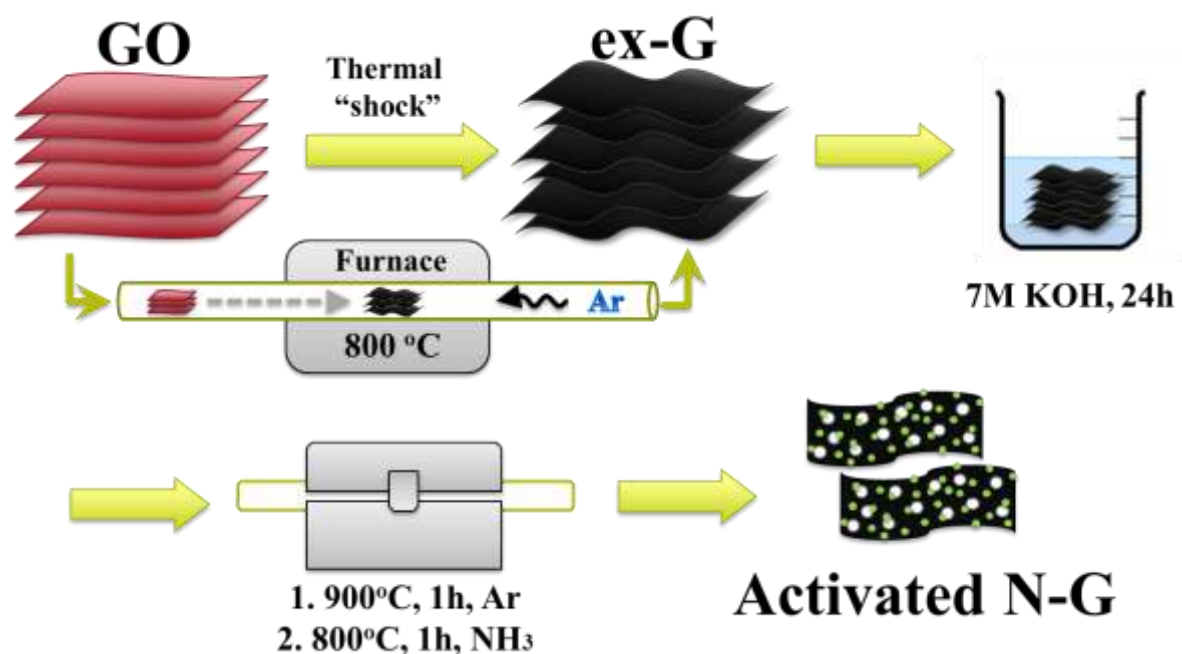


**Figure 26: Schematic representation of activated nitrogen-doped graphene support synthesis**

### 5.2.2 Catalyst Preparation

The Pt supported on nitrogen doped activated graphene catalyst (Pt/N-AG) was prepared by the polyol method, depositing Pt (20 wt. %) on two types of graphene supports in ethylene glycol solvent under 3 h of heat-treatment at 140 °C. The mixture is then filtered and oven dried overnight. The commercial 20 wt. % platinum on Vulcan XC-72 catalyst (Pt/XC72) was used as a reference in order to compare the effect of having different catalyst support.

### 5.2.3 Electrocatalytic Activity Evaluation

The electrocatalytic activity was evaluated in a three-electrode electrochemical cell using a Pine-Instrument's Bipotentiostat AFCBP1, equipped with a speed rotator. The electrode was equipped with a 0.19635 cm<sup>2</sup> glassy carbon surface. All RDE measurements were performed in acidic electrolyte, 0.1 M HClO<sub>4</sub>, using a Ag/AgCl reference electrode at room temperature. To prepare the electrode, 4 mg of sample was dissolved ultrasonically into 2 mL of ethanol before 20 μL of the ink and 10 μL of 0.05% Nafion solution were applied to the glassy carbon disk. The catalyst loading on the glass carbon electrode was approximately 200 μg/cm<sup>2</sup> which makes 40 μg/cm<sup>2</sup> Pt loading. ORR curves were recorded in the potential range at a scan rate of 10 mV/s at various rotation speeds (100, 400, 900, and 1600 rpm) with the electrolyte saturated with oxygen gas. ORR curves were corrected for the background by conducting the same sweep voltammetry in the absence of oxygen and subtracting the curve from the measured ORR curves. The accelerated degradation test (ADT) was conducted by running 1000 cycles in the potential range from 0 V to 1.2 V vs RHE at a scan rate of 50 mV/s in nitrogen saturated electrolyte.

## 5.3 Results and Discussion

In order to evaluate the particle size of the Pt particles deposited on both Pt/XC72 and Pt/N-AG, XRD technique was utilized. The mean platinum particle size for the two catalyst materials can be estimated from Scherrer's equation. Figure 27 shows the diffraction patterns of the different catalysts with the platinum peaks at approx. 39°, 46°, 67° and 81° corresponding to the (111), (200), (220) and (311) faces of platinum, respectively. Particle

size calculations of two catalysts were estimated based on the Pt(220) peak which yielded platinum particle sizes of 2.843 nm and 2.475 nm for Pt/XC72 and Pt/N-AG respectively. The results are summarized in table 6.

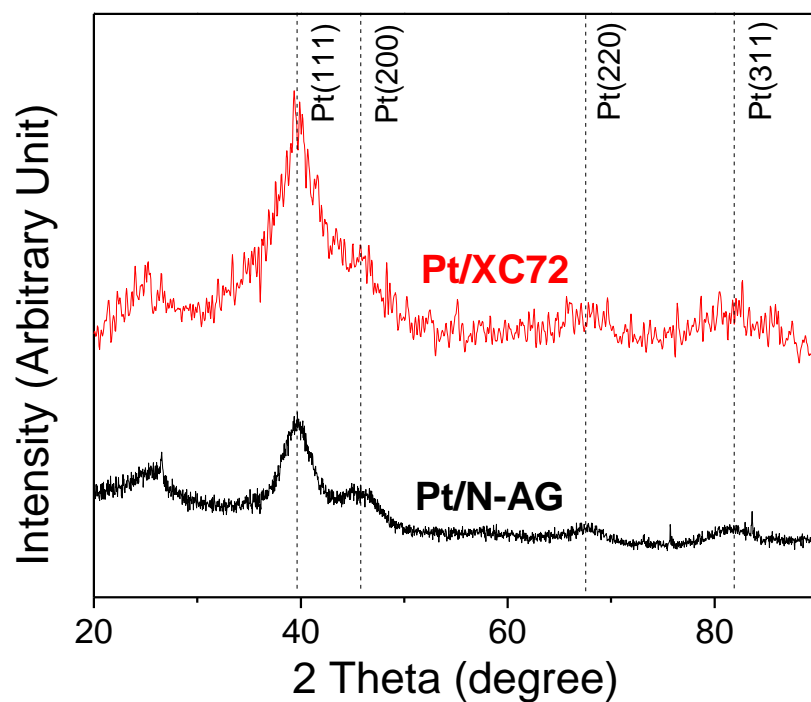


**Figure 27: XRD patterns of Pt/XC72 and Pt/N-AG. Reproduced with permissions from [94]. Copyright © 2012 ECS – The Electrochemical Society**

**Table 6: The mean platinum particle size of Pt/XC72 and Pt/N-AG. Reproduced with permissions from [94]. Copyright © 2012 ECS – The Electrochemical Society**

	<b>2 theta</b>	<b>FWHM</b>	<b>Diameter (nm)</b>
Pt/XC72	67.287	3.317	2.843
Pt/N-AG	67.408	3.814	2.475

To investigate the surface morphology of graphene support used and to confirm the particle size obtained by XRD, Pt/AG and Pt/N-AG were observed by high resolution TEM, shown in Figure 28. The platinum particles added onto the Pt/N-AG catalyst show better dispersion and reasonably uniform particle sizes than that of Pt/AG. Through TEM, the average particle size of platinum on the Pt/N-AG was approximated to be 3 nm which is in reasonable accordance with XRD data. The wrinkles observed in both catalysts suggest the presence of defects created by activation and/or nitrogen-doping of the graphene. In addition, the TEM image of Pt/AG shows more layered structure of graphene and some of the Pt particles in-trapped between those layers, compared to the single layer and clear Pt particles observed in Pt/N-AG. It seems that presence of nitrogen groups on graphene enhances uniform distribution of Pt nanoparticle as well as reducing the wrinkling effect of the graphene, possibly due to the reduced number of defects upon effective deposition of Pt particles on nitrogen-doped graphene.

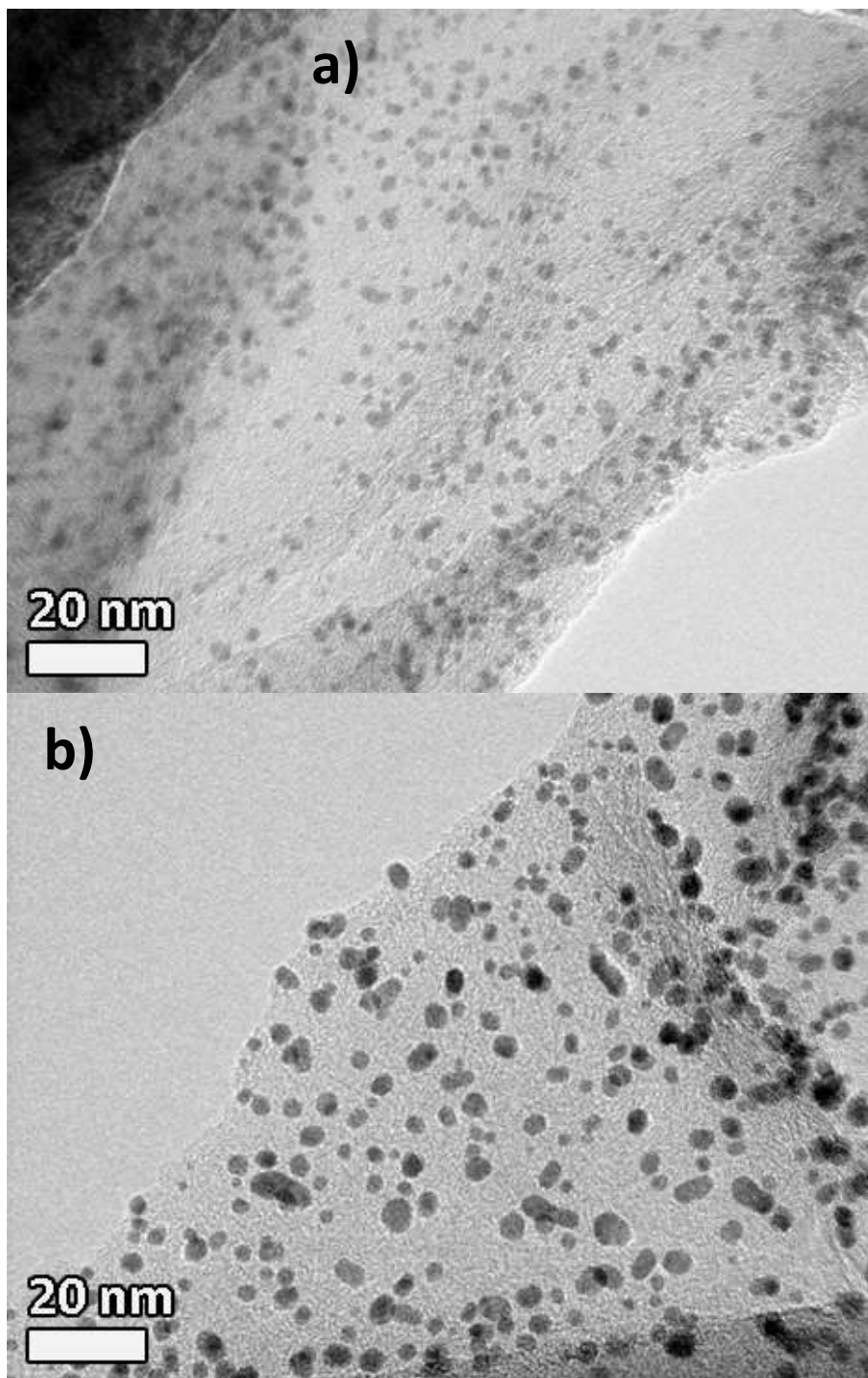


**Figure 28: High resolution TEM images of (a) Pt/AG and (b) Pt/N-AG catalysts illustrating Pt nanoparticles and their distribution on the graphene supports. Reproduced with permissions from [94]. Copyright © 2012 ECS – The Electrochemical Society**

Half-cell RDE experiments were conducted for the two graphene based Pt catalysts to determine their catalytic activity for the ORR as well as for Pt/XC72 as a reference catalyst. These ORR curves with the background currents subtracted are plotted in Figure 29. From the curves, it is shown that the onset-potential of both graphene based catalysts, Pt/AG and Pt/N-AG, are very similar to that of Pt/XC72. In addition, the current density of Pt/N-AG catalyst obtained at 0.8 V is slightly higher than that of the reference catalyst (2.569 mA/cm<sup>2</sup> and 2.585 mA/cm<sup>2</sup> for Pt/XC72 and Pt/N-AG, respectively), although for Pt/AG catalyst, its current density and the limiting current were not as good as the other two curves. This could be due to the reduced conductivity by presence of defects, non-uniform distribution of Pt particles and/or the layered structure and mechanical properties of graphene hindering ORR active sites and their 3-phase reaction. Further investigation will be necessary in order to confirm the causes. However, it is evident that nitrogen doping on the activated graphene can provide a better support material to enhance the ORR performance of Pt catalyst. The ORR performance curves for Pt/N-AG catalyst in various rotating speed are illustrated in Figure 30 along with the Koutecky-Levich plot. The slope from the KL plot gives the number of electrons which turned out to be 3.96, indicating that the reaction is 4-electron pathway dominant and almost no 2-electron pathway is occurring.

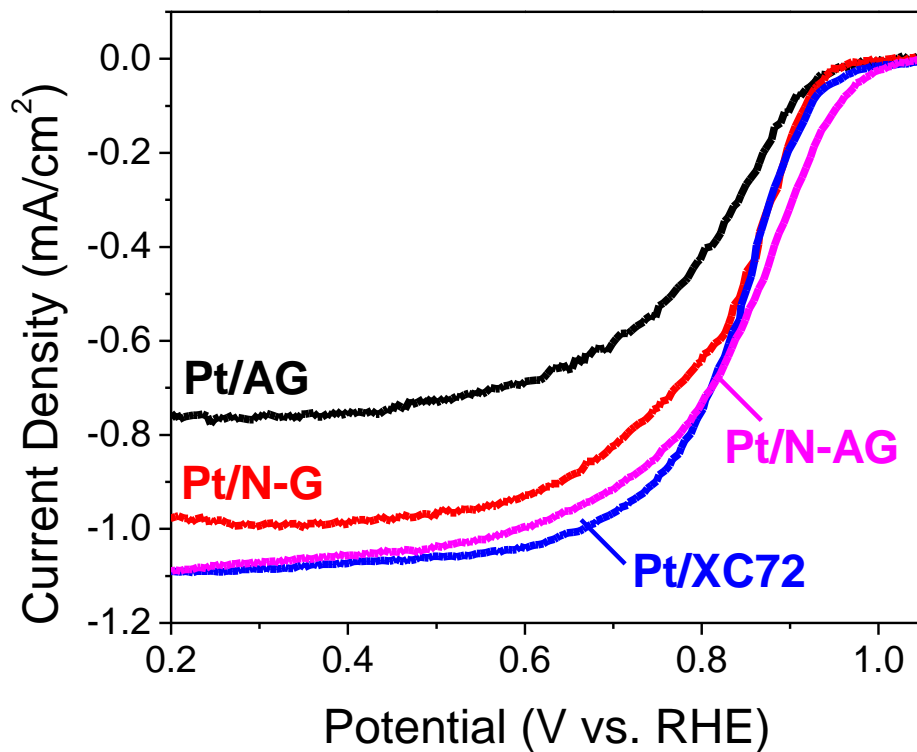
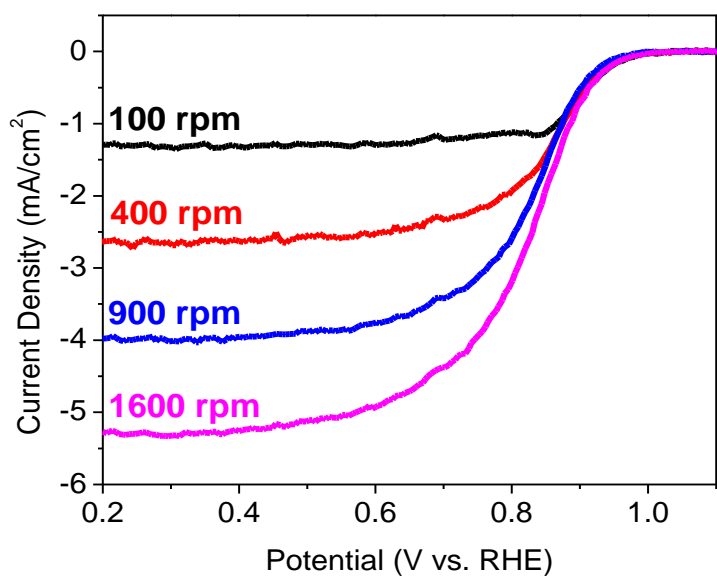


**Figure 29:** ORR curves of Pt catalysts supported on N-AG, AG and XC72 obtained at 900 rpm in oxygen saturated 0.1 M HClO<sub>4</sub> electrolyte with a potential scan rate of 10 mV/s. Reproduced with permissions from [94]. Copyright © 2012 ECS – The Electrochemical Society

a)



b)

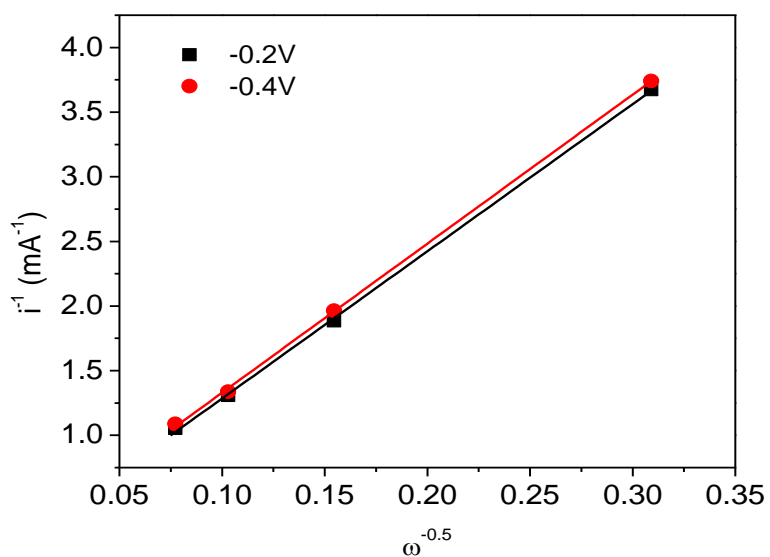


**Figure 30:** a) The ORR performance of Pt/N-AG catalyst in various rotating speed and b) the Koutecky-Levich plot obtained in oxygen saturated 0.1 M HClO<sub>4</sub> electrolyte with a potential scan rate of 10 mV/s. Reproduced with permissions from [94]. Copyright © 2012 ECS – The Electrochemical Society

In addition to the initial ORR performance measure, durability of the Pt/N-AG catalyst was also investigated by accelerated degradation testing (ADT) consisting of 1000 cycles in N<sub>2</sub> saturated electrolyte at a scan rate of 50 mV/s between 0 and 1.2 V vs. RHE. It can be observed from the TEM images of Pt/N-AG and Pt/XC72 catalysts after ADT shown in Figure 31 that most of the Pt particles on N-AG support remained as relatively small particles with even distribution along the surface, while the Pt particles on XC72 surface have undergone agglomeration and dissolution. Durability data of Pt/N-AG and the reference catalyst Pt/XC72 are provided in Figure 32. Pt/N-AG showed slight decrease in the limiting current and almost no evidence of degradation in the onset-potential while Pt/XC72 showed a potential decrease of 0.012 V. At 0.8 V vs. RHE, the decreases in the current densities obtained before and after ADT are 0.369 (14.2%) and 0.839 (32.64%) mA/cm<sup>2</sup> for Pt/N-AG and Pt/XC72 respectively, and this results in the higher percentage drop of mass activity before and after ADT for the Pt/XC72. The mass activity obtained at the same voltage drops by 29.3 % for Pt/N-AG while it is 37.5 % for Pt/XC72. This enhancement in durability is most likely arising due to the nature of graphene material such as high mechanical and chemical stability, rendering N-AG as a promising platinum catalyst support.

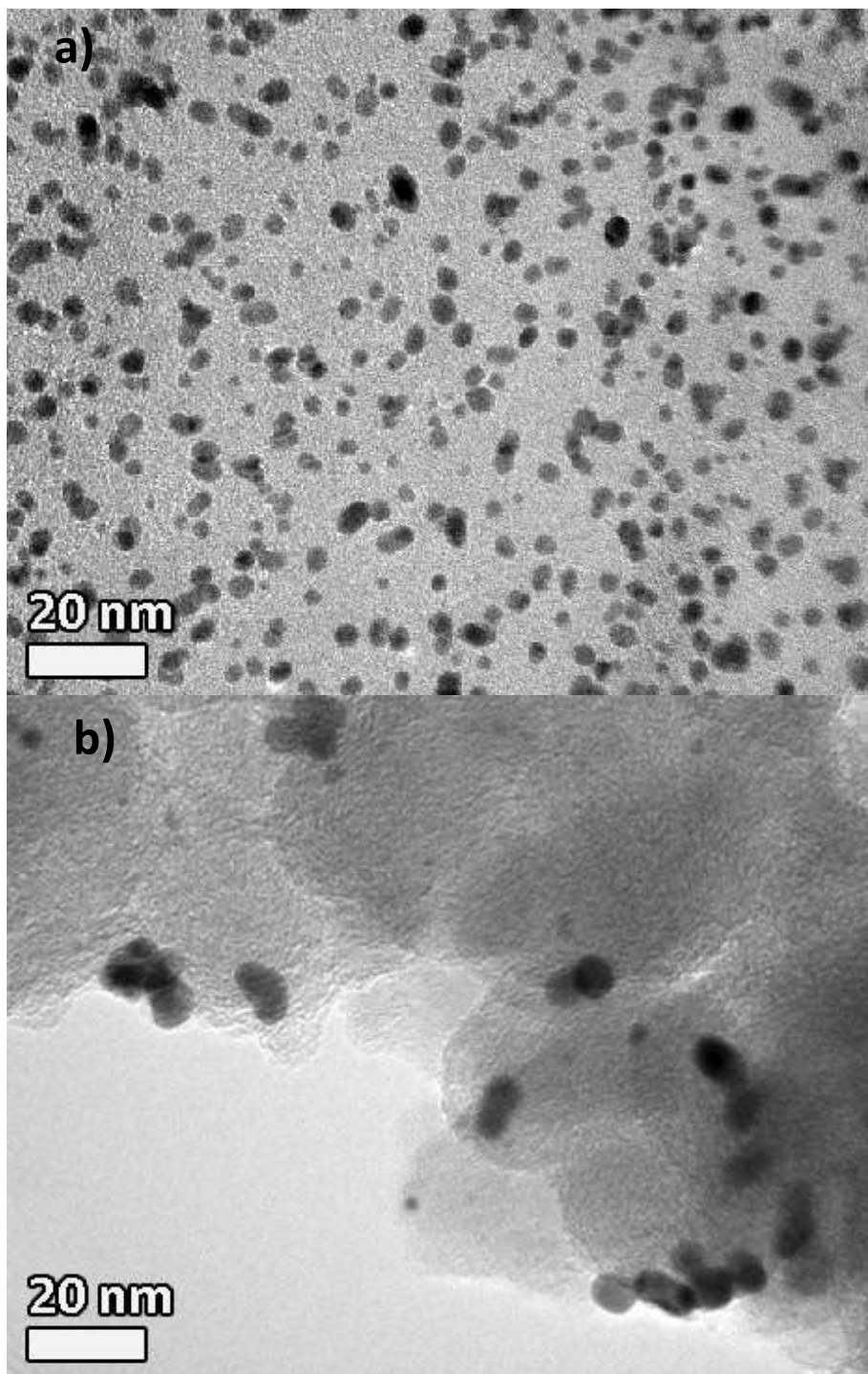


**Figure 31: High resolution TEM images of (a) Pt/N-AG and (b) Pt/XC72 catalysts after accelerated durability test.**

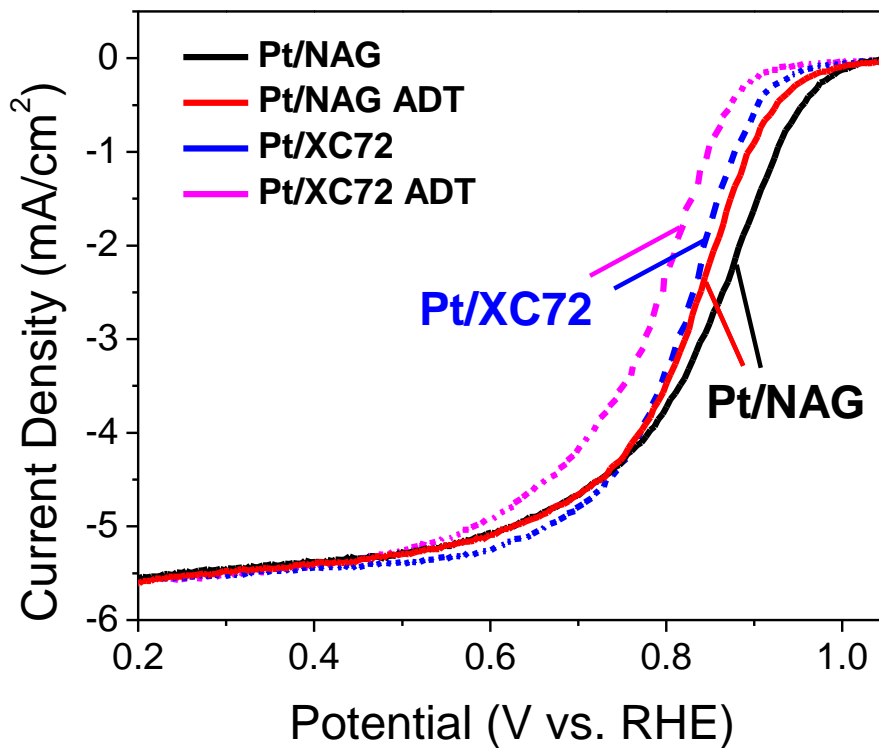


**Figure 32: ORR curves of Pt/N-AG and Pt/XC72 before and after accelerated durability test obtained at 900 rpm in oxygen saturated 0.1 M HClO<sub>4</sub> electrolyte with a potential scan rate of 10 mV/s. Reproduced with permissions from [94]. Copyright © 2012 ECS – The Electrochemical Society**

## 5.4 Conclusions

We have successfully synthesized a platinum nanoparticle catalyst using nitrogen-doped activated graphene as support. Well-dispersed platinum nanoparticles with controlled particle size were found on the functionalized graphene surface. This precious catalyst demonstrates promising electrocatalytic activity and durability for the ORR when compared with the commercial platinum catalyst supported on XC72, rendering graphene as a suitable replacement to traditional nanostructured carbon support materials. Among two types of graphene supports used, Pt on N-AG was found to display optimal ORR activity and durability. The high stability demonstrated through ADT is most likely due to the characteristics of nitrogen-doped graphene as a support material. Thus, graphene is presented as an ideal catalyst support material, with promising ORR activity and stability demonstrated. Future investigations will focus on characterizing the interaction among nitrogen, graphene and platinum nanoparticles as well as to apply the material in other types of fuel cell catalysts.

## Section 6: Summary and Future Work

In summary, three different experiments were carried out to explore three different types of carbon supported ORR catalysts for fuel cell applications. The primary objective was to investigate the contributions of unique physical and chemical properties of different supporting materials to the performance and durability of the fuel cell catalysts. The first two studies focused on developing durable and active NPMCs with mesoporous carbon and graphene nanoplatelet support materials which have been successfully carried out along with in depth analysis on the nitrogen groups related to their performances. The last study has also successfully demonstrated that graphene can be used as active and stable supporting material for Pt catalysts in acid environment.

In the first study, non-precious metal catalysts (NPMC) for the oxygen reduction reaction were synthesized by deposition of Fe/Co-N<sub>x</sub> composite onto nanoporous carbon black with ethylenediamine (EDA) as nitrogen precursor. The results obtained from the optimized FeCo/EDA-carbon catalyst, using KJ600 as the support, showed improved onset, half-wave potentials and superior selectivity than that of the KJ300. Similarly, the catalyst showed good performance in the hydrogen-oxygen PEM fuel cell. The X-ray photoelectron spectroscopy (XPS) study indicated that pyridinic type nitrogen of the non-precious metal catalysts is critical for ORR catalytic activity and selectivity. These results suggest higher pore volume and surface area of carbon support could lead to higher nitrogen content

providing more active sites for ORR and this type of catalyst has great potential used as a non-precious PEM fuel cell catalyst

In the second study, we report the development of a novel NPMC in acid electrolyte using pyrimidine-2,4,5,6-tetramine sulfuric acid hydrate (PTAm) as a nitrogen precursor and graphene nanosheets as catalyst supports. This novel NPMC demonstrates promising electrocatalyst activity and durability superior to that of commercial catalyst for the ORR, rendering graphene nanosheets as a suitable replacement to traditional nanostructured carbon support materials.

In the final study, we have developed Pt catalyst by combining the precious metal with nitrogen-doped activated graphene as the support. The catalyst shows uniform size and distribution of platinum nanoparticles on its graphene surface. This novel catalyst demonstrates superior electrocatalyst activity and durability over Pt/XC72 catalyst for ORR under the studied conditions, rendering graphene as an ideal replacement to traditional nanostructured carbon support materials.

Based on the findings of these studies, some future directions for the catalysts research can be suggested:

1. Perform a complete fuel cell performance test for the catalysts that have been verified by the half-cell test.
2. Synthesis of NPMCs with different nitrogen precursors and metal precursors based on the graphene nanosheet support. Since not much research has been done on

NPMCs with this type of support, various combinations of the currently known precursors will likely lead to a development of active catalysts.

3. Synthesis of NPMCs with two or more support materials mixed together. It has been observed that having graphene nanoplatelets and adequate precursors can effectively form the ORR active sites while having no porous structure on the support. By mixing mesoporous / microporous supporting materials and graphene nanoplatelets may provide more effective areas to form ORR active sites, thus enhancing the overall performance, conductivity, and durability.
4. Alloy the platinum particles on the nitrogen-doped graphene support with other transition metals to enhance the utilization of platinum. Increased surface area and other synergetic effects will likely to increase the performance and the durability.

## References

- [1] B. Thinnies, *Hydrocarb Process* 91 (2012) 17-19.
- [2] S. Shafiee, E. Topal, *Energ Policy* 37 (2009) 181-189.
- [3] F.C. Handbook, Inc. November (2004).
- [4] J. Sinha, S. Lasher, Y. Yang, P. Kopf, *Fuel Cell Tech Team Review* (2008).
- [5] S.J. Ashton, *Design, Construction and Research Application of a Differential Electrochemical Mass Spectrometer (DEMS)*, Springer Berlin Heidelberg, 2012, pp. 1-8.
- [6] J. Zhang, *PEM fuel cell electrocatalysts and catalyst layers: fundamentals and applications*, Springer, 2008.
- [7] J. Wu, X.Z. Yuan, J.J. Martin, H. Wang, J. Zhang, J. Shen, S. Wu, W. Merida, *J Power Sources* 184 (2008) 104-119.
- [8] L. Zhang, J. Zhang, D.P. Wilkinson, H. Wang, *J Power Sources* 156 (2006) 171-182.
- [9] C.W.B. Bezerra, L. Zhang, K. Lee, H. Liu, A.L.B. Marques, E.P. Marques, H. Wang, J. Zhang, *Electrochim Acta* 53 (2008) 4937-4951.
- [10] E. Antolini, *Applied Catalysis B: Environmental* 74 (2007) 337-350.
- [11] H.R. Colón-Mercado, B.N. Popov, *J Power Sources* 155 (2006) 253-263.
- [12] Q. He, S. Mukerjee, *Electrochim Acta* 55 (2010) 1709-1719.
- [13] Y. Zhou, K. Neyerlin, T.S. Olson, S. Pylypenko, J. Bult, H.N. Dinh, T. Gennett, Z. Shao, R. O'Hayre, *Energ Environ Sci* 3 (2010) 1437-1446.

- [14] P. Mani, R. Srivastava, P. Strasser, *J Power Sources* 196 (2011) 666-673.
- [15] H. Niwa, K. Horiba, Y. Harada, M. Oshima, T. Ikeda, K. Terakura, J.-i. Ozaki, S. Miyata, *J Power Sources* 187 (2009) 93-97.
- [16] M.S. Wilson, S. Gottesfeld, *J Electrochem Soc* 139 (1992) L28-L30.
- [17] R. O'Hayre, S.-J. Lee, S.-W. Cha, F.B. Prinz, *J Power Sources* 109 (2002) 483-493.
- [18] D. Gruber, N. Ponath, J. Müller, F. Lindstaedt, *J Power Sources* 150 (2005) 67-72.
- [19] B. Wang, *J Power Sources* 152 (2005) 1-15.
- [20] R. Jasinski, (1964).
- [21] M. Lefèvre, E. Proietti, F. Jaouen, J.-P. Dodelet, *Science (New York, N.Y.)* 324 (2009) 71-74.
- [22] X. Li, G. Liu, B.N. Popov, *J Power Sources* 195 (2010) 6373-6378.
- [23] H. Meng, N. Larouche, M. Lefevre, F. Jaouen, B. Stansfield, J.P. Dodelet, *Electrochim Acta* 55 (2010) 6450-6461.
- [24] W.M. Li, A.P. Yu, D.C. Higgins, B.G. Llanos, Z.W. Chen, *J Am Chem Soc* 132 (2010) 17056-17058.
- [25] T. Palaniselvam, R. Kannan, S. Kurungot, *Chem Commun* 47 (2011) 2910-2912.
- [26] G. Wu, K.L. More, C.M. Johnston, P. Zelenay, *Science* 332 (2011) 443-447.
- [27] D. Ohms, S. Herzog, R. Franke, V. Neumann, K. Wiesener, S. Gamburgcev, A. Kaisheva, I. Iliev, *J Power Sources* 38 (1992) 327-334.
- [28] A. Widelöv, R. Larsson, *Electrochim Acta* 37 (1992) 187-197.

- [29] R. Jiang, D. Chu, *J Electrochem Soc* 147 (2000) 4605-4609.
- [30] J. Maruyama, I. Abe, *J Electrochem Soc* 154 (2007) B297-B304.
- [31] D. Chu, R. Jiang, *Solid State Ionics* 148 (2002) 591-599.
- [32] K. Lee, L. Zhang, H. Lui, R. Hui, Z. Shi, J. Zhang, *Electrochim Acta* 54 (2009) 4704-4711.
- [33] M. Manzoli, R.D. Monte, F. Boccuzzi, S. Coluccia, J. Kašpar, *Applied Catalysis B: Environmental* 61 (2005) 192-205.
- [34] P. He, M. Lefevre, G. Faubert, J. Dodelet, *Journal of new materials for electrochemical systems* 2 (1999) 243-252.
- [35] S. Gupta, D. Tryk, I. Bae, W. Aldred, E. Yeager, *Journal of applied electrochemistry* 19 (1989) 19-27.
- [36] K. Sawai, N. Suzuki, *J Electrochem Soc* 151 (2004) A682-A688.
- [37] P.H. Matter, L. Zhang, U.S. Ozkan, *J Catal* 239 (2006) 83-96.
- [38] R. Bashyam, P. Zelenay, *Nature* 443 (2006) 63-66.
- [39] J.Y. Choi, R.S. Hsu, Z.W. Chen, *J Phys Chem C* 114 (2010) 8048-8053.
- [40] G. Liu, X. Li, P. Ganesan, B.N. Popov, *Electrochim Acta* 55 (2010) 2853-2858.
- [41] V. Nallathambi, J.-W. Lee, S.P. Kumaraguru, G. Wu, B.N. Popov, *J Power Sources* 183 (2008) 34-42.
- [42] N.P. Subramanian, S.P. Kumaraguru, H. Colon-Mercado, H. Kim, B.N. Popov, T. Black, D.A. Chen, *J Power Sources* 157 (2006) 56-63.
- [43] B.N. Popov, X. Li, G. Liu, J.-W. Lee, *Int J Hydrogen Energ* 36 (2011) 1794-1802.

- [44] T.E. Wood, Z. Tan, A.K. Schmoeckel, D. O'Neill, R. Atanasoski, *J Power Sources* 178 (2008) 510-516.
- [45] G. Wu, C.M. Johnston, N.H. Mack, K. Artyushkova, M. Ferrandon, M. Nelson, J.S. Lezama-Pacheco, S.D. Conradson, K.L. More, D.J. Myers, P. Zelenay, *J Mater Chem* (2011).
- [46] R. Cote, G. Lalande, G. Faubert, D. Guay, J. Dodelet, G. Denes, *Journal of new materials for electrochemical systems* 1 (1998) 7-16.
- [47] M.M. Alves, J. Dodelet, D. Guay, M. Ladouceur, G. Tourillon, *The Journal of Physical Chemistry* 96 (1992) 10898-10905.
- [48] A. Bouwkamp-Wijnoltz, W. Visscher, J. Van Veen, S. Tang, *Electrochim Acta* 45 (1999) 379-386.
- [49] G. Faubert, R. Cote, D. Guay, J. Dodelet, G. Denes, P. Bertrandc, *Electrochim Acta* 43 (1998) 341-353.
- [50] X. Wang, J.S. Lee, Q. Zhu, J. Liu, Y. Wang, S. Dai, *Chemistry of Materials* 22 (2010) 2178-2180.
- [51] M. Bron, S. Fiechter, M. Hilgendorff, P. Bogdanoff, *Journal of applied electrochemistry* 32 (2002) 211-216.
- [52] F. Jaouen, S. Marcotte, J.-P. Dodelet, G. Lindbergh, *The Journal of Physical Chemistry B* 107 (2003) 1376-1386.
- [53] M. Lefevre, J. Dodelet, P. Bertrand, *The Journal of Physical Chemistry B* 109 (2005) 16718-16724.
- [54] M. Lefèvre, J.-P. Dodelet, *Electrochim Acta* 48 (2003) 2749-2760.
- [55] C. Medard, M. Lefevre, J. Dodelet, F. Jaouen, G. Lindbergh, *Electrochim Acta* 51 (2006) 3202-3213.
- [56] F. Charreteur, F. Jaouen, J.-P. Dodelet, *Electrochim Acta* 54 (2009) 6622-6630.

- [57] Z. Wen, J. Liu, J. Li, *Advanced Materials* 20 (2008) 743-747.
- [58] S.H. Joo, C. Pak, D.J. You, S.-A. Lee, H.I. Lee, J.M. Kim, H. Chang, D. Seung, *Electrochim Acta* 52 (2006) 1618-1626.
- [59] E.P. Ambrosio, C. Francia, M. Manzoli, N. Penazzi, P. Spinelli, *Int J Hydrogen Energ* 33 (2008) 3142-3145.
- [60] J.B. Joo, P. Kim, W. Kim, J. Kim, J. Yi, *Catalysis Today* 111 (2006) 171-175.
- [61] Z. Chen, D. Higgins, H. Tao, R.S. Hsu, Z. Chen, *The Journal of Physical Chemistry C* 113 (2009) 21008-21013.
- [62] K. Gong, F. Du, Z. Xia, M. Durstock, L. Dai, *Science* 323 (2009) 760-764.
- [63] D.C. Higgins, D. Meza, Z.W. Chen, *J Phys Chem C* 114 (2010) 21982-21988.
- [64] W. Li, C. Liang, W. Zhou, J. Qiu, Zhou, G. Sun, Q. Xin, *The Journal of Physical Chemistry B* 107 (2003) 6292-6299.
- [65] Y. Lin, X. Cui, C. Yen, C.M. Wai, *The Journal of Physical Chemistry B* 109 (2005) 14410-14415.
- [66] W. Zhang, P. Sherrell, A.I. Minett, J.M. Razal, J. Chen, *Energ Environ Sci* 3 (2010) 1286-1293.
- [67] J. Guo, G. Sun, Q. Wang, G. Wang, Z. Zhou, S. Tang, L. Jiang, B. Zhou, Q. Xin, *Carbon* 44 (2006) 152-157.
- [68] S. Maldonado, K.J. Stevenson, *The Journal of Physical Chemistry B* 109 (2005) 4707-4716.
- [69] K. Lee, J. Zhang, H. Wang, D.P. Wilkinson, *Journal of applied electrochemistry* 36 (2006) 507-522.
- [70] Y. Shao, J. Liu, Y. Wang, Y. Lin, *J Mater Chem* 19 (2009) 46-59.

- [71] E. Antolini, E.R. Gonzalez, *Solid State Ionics* 180 (2009) 746-763.
- [72] M.S. Saha, R. Li, X. Sun, *Electrochem Commun* 9 (2007) 2229-2234.
- [73] X. Chen, S.S. Mao, *ChemInform* 38 (2007) no-no.
- [74] S.H. Lee, R. Deshpande, P.A. Parilla, K.M. Jones, B. To, A.H. Mahan, A.C. Dillon, *Advanced Materials* 18 (2006) 763-766.
- [75] M.K. Jeon, H. Daimon, K.R. Lee, A. Nakahara, S.I. Woo, *Electrochem Commun* 9 (2007) 2692-2695.
- [76] D.J. Ham, Y.K. Kim, S.H. Han, J.S. Lee, *Catalysis Today* 132 (2008) 117-122.
- [77] X. Sun, R. Li, D. Villers, J.P. Dodelet, S. Désilets, *Chemical Physics Letters* 379 (2003) 99-104.
- [78] J. Lee, J. Kim, T. Hyeon, *Advanced Materials* 18 (2006) 2073-2094.
- [79] L. Zhang, J. Niu, L. Dai, Z. Xia, *Langmuir* 28 (2012) 7542-7550.
- [80] C.H. Choi, S.Y. Lee, S.H. Park, S.I. Woo, *Applied Catalysis B: Environmental* 103 (2011) 362-368.
- [81] J. Goldstein, D.E. Newbury, D.C. Joy, C.E. Lyman, P. Echlin, E. Lifshin, L. Sawyer, J.R. Michael, *Scanning electron microscopy and X-ray microanalysis*, Springer, 2003.
- [82] H. Seiler, *J Appl Phys* 54 (1983) R1-R18.
- [83] M.A. Sutton, N. Li, D.C. Joy, A.P. Reynolds, X. Li, *Exp Mech* 47 (2007) 775-787.
- [84] D.B. Williams, C.B. Carter, *The Transmission Electron Microscope*, Springer, 1996.
- [85] D.B. Williams, C.B. Carter, *Transmission Electron Microscopy*, Springer, 2009, pp. 3-22.

- [86] D. Alloyeau, in: D. Alloyeau, C. Mottet, C. Ricolleau (Eds.), *Nanoalloys*, Springer London, 2012, pp. 113-157.
- [87] B.E. Warren, *X-ray Diffraction*, Courier Dover Publications, 1969.
- [88] L.V. Azároff, R. Kaplow, N. Kato, R.J. Weiss, A. Wilson, R. Young, *X-ray Diffraction*, McGraw-Hill New York, 1974.
- [89] C. Fadley, S. Davison, Vol. 16 *Pergamon, New York* (1984) 275.
- [90] C. Fadley, R. Baird, W. Siekhaus, T. Novakov, S. Bergström, *Journal of Electron Spectroscopy and Related Phenomena* 4 (1974) 93-137.
- [91] D.W. Turner, M.A. Jobory, *The Journal of Chemical Physics* 37 (1962) 3007-3008.
- [92] S. Brunauer, P.H. Emmett, E. Teller, *J Am Chem Soc* 60 (1938) 309-319.
- [93] W. Schmickler, E. Santos, *Interfacial Electrochemistry*, Springer Berlin Heidelberg, 2010, pp. 259-267.
- [94] J.-Y. Choi, D.U. Lee, Z. Chen, *Ecs Transactions* 50 (2013) 1815-1822.
- [95] M. Lefevre, J. Dodelet, P. Bertrand, *J. Phys. Chem. B* 104 (2000) 11238-11247.
- [96] H. Liu, C. Song, Y. Tang, J. Zhang, *Electrochim Acta* 52 (2007) 4532-4538.
- [97] G. Lalande, R. Cote, D. Guay, J. Dodelet, L. Weng, P. Bertrand, *Electrochim Acta* 42 (1997) 1379-1388.
- [98] R. Cote, G. Lalande, D. Guay, J. Dodelet, G. Denes, *J Electrochem Soc* 145 (1998) 2411.
- [99] P. Guerec, M. Savy, J. Riga, *Electrochim. Acta* 43 (1998) 743-753.
- [100] S. Gojkovi , S. Gupta, R. Savinell, *J Electroanal Chem* 462 (1999) 63-72.

- [101] P. Gouerec, M. Savy, *Electrochim Acta* 44 (1999) 2653-2661.
- [102] H. Schulenburg, S. Stankov, V. Schunemann, J. Radnik, I. Dorbandt, S. Fiechter, P. Bogdanoff, H. Tributsch, *J. Phys. Chem. B* 107 (2003) 9034-9041.
- [103] S. Marcotte, D. Villers, N. Guillet, L. Roue, J. Dodelet, *Electrochim Acta* 50 (2004) 179-188.
- [104] K. Sawai, N. Suzuki, *J Electrochem Soc* 151 (2004) A2132.
- [105] D. Villers, X. Jacques-Bard, J. Dodelet, *J Electrochem Soc* 151 (2004) A1507.
- [106] S. Yamazaki, Y. Yamada, T. Ioroi, N. Fujiwara, Z. Siroma, K. Yasuda, Y. Miyazaki, *J Electroanal Chem* 576 (2005) 253-259.
- [107] M. Lefevre, E. Proietti, F. Jaouen, J. Dodelet, *Science* 324 (2009) 71.
- [108] F. Jaouen, M. Lefevre, J. Dodelet, M. Cai, *J. Phys. Chem. B* 110 (2006) 5553-5558.
- [109] F. Charreteur, F. Jaouen, S. Ruggeri, J. Dodelet, *Electrochim Acta* 53 (2008) 2925-2938.
- [110] V. Nallathambi, J. Lee, S. Kumaraguru, G. Wu, B. Popov, *J Power Sources* 183 (2008) 34-42.
- [111] Y. Hong, Y. Rheem, M. Lai, D. Cwiertny, S. Walker, N. Myung, *Chemical Engineering Journal* 151 (2009) 66-72.
- [112] J. Liu, R. Czerw, D. Carroll, *Journal of Materials Research* 20 (2005) 538.
- [113] S. Maldonado, S. Morin, K. Stevenson, *Carbon* 44 (2006) 1429-1437.
- [114] X. Li, S. Park, B.N. Popov, *J Power Sources* 195 (2010) 445-452.
- [115] Z.W. Chen, D.C. Higgins, A. Yu, L. Zhang, J. Zhang, *Energy Environ. Sci.* (2011).

- [116] R. Baker, D.P. Wilkinson, J. Zhang, *Electrochim Acta* 53 (2008) 6906-6919.
- [117] F. Jaouen, E. Proietti, M. Lefevre, R. Chenitz, J.-P. Dodelet, G. Wu, H.T. Chung, C.M. Johnston, P. Zelenay, *Energ Environ Sci* 4 (2011) 114-130.
- [118] A.K. Geim, K.S. Novoselov, *Nat Mater* 6 (2007) 183-191.
- [119] S. Yang, X. Feng, X. Wang, K. Müllen, *Angewandte Chemie* 50 (2011) 5339-5343.
- [120] D.S. Geng, Y. Chen, Y.G. Chen, Y.L. Li, R.Y. Li, X.L. Sun, S.Y. Ye, S. Knights, *Energ Environ Sci* 4 (2011) 760-764.
- [121] Y.Q. Sun, C. Li, Y.X. Xu, H. Bai, Z.Y. Yao, G.Q. Shi, *Chem Commun* 46 (2010) 4740-4742.
- [122] J.-Y. Choi, D. Higgins, Z. Chen, *J Electrochem Soc* 159 (2011) B86-B89.
- [123] R.D.L. Smith, P.G. Pickup, *Electrochem Commun* 11 (2009) 10-13.
- [124] F. Jaouen, J. Herranz, M. Lefèvre, J.-P. Dodelet, U.I. Kramm, I. Herrmann, P. Bogdanoff, J. Maruyama, T. Nagaoka, A. Garsuch, J.R. Dahn, T. Olson, S. Pylypenko, P. Atanassov, E.a. Ustinov, *ACS applied materials & interfaces* 1 (2009) 1623-1639.
- [125] M. Lefevre, J.P. Dodelet, P. Bertrand, *J Phys Chem B* 106 (2002) 8705-8713.
- [126] F. Charreteur, F. Jaouen, S. Ruggeri, J.P. Dodelet, *Electrochim Acta* 53 (2008) 2925-2938.
- [127] L. Qu, Y. Liu, J.-B. Baek, L. Dai, *ACS Nano* 4 (2010) 1321-1326.
- [128] H.C. Schniepp, J.-L. Li, M.J. McAllister, H. Sai, M. Herrera-Alonso, D.H. Adamson, R.K. Prud'homme, R. Car, D.A. Saville, I.A. Aksay, *The Journal of Physical Chemistry B* 110 (2006) 8535-8539.

## Appendix

Published papers have been used in this thesis. The permissions to reuse the published work have been requested and granted.

### Publications

Highly Active Porous Carbon-Supported Nonprecious Metal–N Electrocatalyst for Oxygen Reduction Reaction in PEM Fuel Cells

**Choi, J.**; Hsu, R.S.; Chen, Z. W.

The Journal of Physical Chemistry C, 2010, 114 (17), 8048–8053

<http://pubs.acs.org/doi/abs/10.1021/jp910138x>

Highly Durable Graphene Nanosheet Supported Iron Catalyst for Oxygen Reduction Reaction in PEM Fuel Cells

**Choi, J.**; Higgins, D. C.; Chen, Z. W.

Journal of The Electrochemical Society, 2012, 159 (1), B87

<http://jes.ecsdl.org/content/159/1/B86>

Nitrogen-doped Activated Graphene Supported Platinum Electrocatalyst for Oxygen Reduction Reaction in PEM Fuel Cells

**Choi, J.**; Lee, D.; Chen, Z. W.

ECS Transactions, 2012, 50 (2), 1815-1822

<http://ecst.ecsdl.org/content/50/2/1815.abstract>